BUREAU TECHNIQUE ZBOROWSKI

1, avenue d'Orléans, BRUNOY (Seine-et-Oise) — France

INTERIM TECHNICAL REPORT

DECEMBER, 1961

THEORETICAL INVESTIGATION AND CONTROL BY MEASURING TESTS ON THE BEHAVIOR OF THE THREE-DIMENSIONAL TURBULENT BOUNDARY LAYER ON AN ANNULAR WING AT VARIOUS INCIDENCES

By

Ernest A. Eichelbrenner[1]

in collaboration with

Serge Angioletti[2], Yves M. Grellier[3], Rolf S. Hellerström[4]

Prepared for the

OFFICE OF NAVAL RESEARCH, AIR PROGRAMS BRANCH
Washington, D. C.

Under Contrat Number : N 62558-2526

1 *Professeur à la Faculté des Sciences de l'Université de Poitiers*
2 *Ingénieur Chef du Groupe de Recherches au BTZ*
3 *Maître-assistant à la Faculté des Sciences de l'Université de Poitiers*
4 *Ingénieur de Recherches au BTZ*

Table of Contents

	Pages.
0. Introduction	3
1. Wall Streamlines in Turbulent Flow	5
2. Separation and Reattachment in Turbulent Flow	8
3. Separation and Reattachment on Ring Airfoils	11
4. Conclusion	17
5. Bibliography	17
6. List of Symbols	18
7. List of Tables	19
8. List of Figures	19
9. Annex	20

Tables 3.1 — 3.4.3
Fig. 0.1 — D 3
Graphs I and II

0. Introduction

0.1. The behavior of three-dimensional boundary layers in laminar flow has been the object of a certain number of theoretical and experimental studies, which lead — at least for predominantly convex obstacles — to a fairly good possibility of predicting the essential features (velocity distribution, stability and separation) of the viscous flow over finite bodies in an air stream. In particular, a research group of ONERA (France) has elaborated, since 1954, a method of theoretical treatment of laminar boundary layers in three dimensions which permits even numerical computations of remarkable accuracy, cf. [1], [2].

0.2. This method is based on two essential assumptions, which restrict to a certain extent the choice of the obstacles to be admitted :

0.2.1. The viscous flow diverges appreciably from the inviscid flow on the edge of the boundary layer only in the immediate neighbourhood of separated-flow regions on the body's surface (principle of prevalence).

0.2.2. The streamlines of the flow inside the boundary layer have well-defined limiting positions for $n \longrightarrow 0$ (n = distance from the wall of the obstacle). These limiting positions will be called "wall streamlines". Except for a (normally finite) number of singular points, each point of the body's surface admits one and only one wall streamline (hypothesis of regularity).

0.3. The first of these two assumptions permits a reduction of the rank of the system of NAVIER-STOKES, by the introduction of curvilinear coordinates (s, z) based on the streamlines of the inviscid flow (see *figure* 0.1).

The second of these assumptions furnishes a particularly useful means of description and analysis of flow configurations on the surface of the obstacle.

0.4. With the help of the conception of "wall streamlines", the trace of a separated area on the body surface ("separation line") can be described, in laminar flow, as a limit of wall streamlines (and therefore as a — singular — wall streamline itself).

0.4.1. Such a singular wall streamline passes, by necessity, through a point of divergence ("separation point"), i.e. a singular point admitting at least *two* wall streamlines.

0.4.2. Its determination is, therefore, possible, if one disposes of a formula characterizing the wall streamlines analytically. Starting from a separation point (necessary condition : $\left(\frac{\partial \vec{V}}{\partial n}\right)_p = 0$, where $\vec{V}$ is the flow vector inside the boundary layer; the index p indicates here and later on the conditions at the wall — in French "paroi", $n = 0$ —), one can find by a step-by-step process the singular wall streamline, i.e. the separation line.

0.5. The required analytical formula has been given by OUDART in 1956 (see [3]) :

0.5.1. If we call θ (n) the angle between the direction of the flow at the outer edge of the boundary layer and the direction of the flow inside it at a distance n from the wall, the value $\theta_p = 0$ (0) characterizes the direction of the wall streamline passing by a given point (s, z) of the surface.

0.5.2. It can easily be shown (§ 1.4.2.) that in laminar flow

$$\operatorname{cotg} \theta_p = c_L \cdot \frac{\Lambda + 12}{\Lambda} \cdot \frac{\frac{\partial K_p}{\partial s} - c_1}{\frac{\partial K_p}{\partial z} - c_2}$$

where Λ is the laminar form parameter of the longitudinal (*) flow, calculated after POHLHAUSEN, and K_p the pressure coefficient $\frac{p - p_\infty}{q_\infty}$. c_1 and c_2 are constants, the values of which depend on the geometry and the position of the obstacle :

We find for instance $c_2 = 0$ for obstacles having a plane of symmetry with respect to the oncoming flow; we find $c_1 = 0$ for all kinds of ellipsoids.

c_L is a universal constant which depends on the degrees k_1 and k_2 of the polynomials representing longitudinal and transversal flow. For $k_1 = k_2 = 4$, as usual in the POHLHAUSEN method, we find $c_L = 1$.

0.5.3. This theory allows very farreaching predictions for the flow configuration e.g. on a flattened ellipsoid with incidence, predictions which have been checked and confirmed by experiment [3], [4] (**). It can therefore be considered as well established and consistent with the physical reality.

0.6. The laminar problem thus being solved, it seems worth while to try an analogous treatment of the turbulent case.

Unfortunately, even in two-dimensional flow, the turbulent boundary layer admits no analytical representation in a simple form which would be equally valid near the wall (i.e. for friction and separation phenomena) and towards the outer edge.

A purely theoretical treatment of the three-dimensional turbulent boundary layer, as in the laminar case, therefore seems — at least for the moment — impossible; experimental evidence will be needed to a far greater extent to guide the theory.

0.7. The BTZ (Bureau Technique Zborowski, Brunoy, France) made in 1958/59 a series of experimental and theoretical investigations in order to improve, by a suitable adaptation of the leading edge, the behavior of ring airfoils at high lift coefficients [5].

0.7.1. It was found that the unsatisfactory form of the lift-drag polar at higher incidences was chiefly due to the development of an important separation bubble forming, on the upper side of the airfoil, behind the leading edge.

(*) i.e. in direction of the streamlines at the outer edge of the boundary layer; the corresponding normal direction defines the "crossflow" or "transversal" flow.

(**) In particular, a very characteristic change with incidence of the flow configuration and, consequently, the existence of a "critical incidence" has been correctly predicted.

0.7.2. As a particularly unfavorable configuration, there has been disclosed the completely stalled flow over the upper side of the ring airfoil, after reunion of this leading-edge separation-bubble with the spreading trailing-edge separation, at a precise (the "critical") incidence.

0.7.3. In order to combat this phenomenon and to prevent (or push back to higher incidences) the reunion of the two separated regions on the ring airfoil, it proved necessary to undertake a more detailed theoretical and experimental study of the features — and if possible of the means of determination — of these separated regions.

0.8. Now, the concerned area of viscous flow over the upper side of the ring airfoil — in the wake of a leading-edge separation-bubble — is a region of reattached and therefore predominantly * turbulent flow.

0.8.1. Thus, BTZ was led, by this problem of practical engineering, to a closer investigation of the behavior and, if possible, of the determination of flow configurations in three-dimensional turbulent boundary layers with regions of reattachment and of separation of the flow.

0.8.2. This investigation has been made possible thanks to the sponsorship of the Office of Naval Research of the United States, sponsorship which permitted a careful analysis of the problem. The theoretical work and its coordination with experiments have been assumed by BTZ: the experimental work has been executed in the "Laboratoire de Mécanique des Fluides" of the University of Poitiers (France).

0.9. The research, very naturally, comprises three phases :

0.9.1. Phase 1 : Analysis of the general features of three-dimensional turbulent boundary layers and, in particular, of the rôle of wall streamlines in the behavior of a turbulent viscous flow over finite bodies.

Establishment and control of a suitable analytical expression for these wall streamlines : Chapter 1 of this report.

0.9.2. Phase 2 : Study of characteristic configurations (reattachment and separation) and their interpretation with the help of the wall-streamlines concept.

Experimental confirmation of this interpretation by visualization of wall streamlines in the critical regions : Chapter 2.

0.9.3. Phase 3 : Application of the results of the two foregoing phases to the numerical determination of the viscous turbulent flow over ring airfoils of different aspect ratios.

Determination and calculation of the critical incidence as contact of separated areas at leading and trailing edge for the considered airfoils.

Extrapolation of the results to wings of infinite aspect ratio (plane wings) and confrontation with already existing measurements on these latter : Chapter 3.

0.10. The theory could be brought to a fairly close agreement with the experimental work presented in this report. The shortcomings are to be attributed to the present state of knowledge about turbulent viscous flow in general.

In the conclusion, an approach to this latter problem, at least on the scale of engineering demands, will be sketched out for future investigations.

0.11. The author wishes to thank, for valuable help in his work, the staff of BTZ and in particular Mr. Serge Angioletti and Mr. Rolf Hellerström. The experimental part has been executed, with skill and tenacity, by Mr. Yves Grellier, Assistant at the Faculty of Sciences of the University of Poitiers.

For critical and constructive discussions of the various problems, the author is deeply indebted to Dr. J. J. Cornish (Mississippi State University), Dr. D. C. Hazen (Princeton University), Dr. B. G. Newman (Mac Gill University) and Dr. I. H. C. Nicholl (Laval University).

The author wishes, last but not least, to acknowledge the helpful interest and the stimulating encouragement of Dr. G. B. Matthews, LCDR A. Van Tuyl and Mr. T. Wilson of the Office of Naval Research.

(*) Regions of more or less extended laminar reattachment may be observed near the corners of the leading-edge bubble, where the corresponding Reynolds number $\mathcal{R}_{\delta_1}$ is below the critical value 450, cf. §§ 3.10.2.2.2 and 3.12.1, fig. 3.19 and photos A7, A8, B7.

1. Wall Streamlines in Turbulent Flow

1.0. In the wall-near portions of turbulent boundary layers, the condition of non-slip at the wall — equally valid for the main flow and for the turbulent fluctuations (u', v', w') — leads to $u' \sim v' \sim w' \sim 0$. The flow therefore shows, in the neighbourhood of the wall of an obstacle, the behavior and the features of a laminar layer. It is called, consequently, the "laminar sublayer".

Wall friction and related phenomena, as separation and reattachment, are located in this sublayer and therefore ruled by its properties. They will then obey analogous laws as in the case of laminar boundary layers. In particular, they will find their expression in a similar behavior of the viscous streamlines as n approaches zero.

1.1. As in the laminar case — and with the same consequences — we can therefore make the following hypotheses :

1.1.1. The viscous flow diverges appreciably from the inviscid flow on the edge of the boundary layer only in the immediate neighbourhood of separated-flow regions on the surface of an obstacle (principle of prevalence).

1.1.2. The streamlines of the flow inside the boundary layer have welldefined limiting positions for $n \to 0$, which will be called "wall streamlines" (hypothesis of regularity).

1.2. As a mere inference from the assumption of a laminar sublayer on the surface of an obstacle, the second hypothesis in particular needs an experimental confirmation, which has been attempted in the low-speed windtunnel of Eiffel-Type at POITIERS (*) on a wooden model of an ellipsoid of revolution.

1.2.1. This model with an axis ratio of 1 : 6 and a great axis of 2 m has been put at the Laboratoire's disposal by the ONERA. The inviscid flow over it can be analytically determined, for all incidences, according to [6]; for an incidence of $i = 10°$, this determination has been numerically executed in [1]. The boundary-layer theory provided already, for this case, the lines of laminar separation and of transition, cf. [3].

1.2.2. At an air speed of 45 m/s and therefore a Reynolds number of $\sim 6.10^6$, the transition line is located — at least on the flanks and on the underside of the obstacle — upstream from the laminar separation line. An appreciable portion of the viscous flow over the body will therefore be turbulent; separation will occur, in these regions, still farther downstream than in the laminar case, turbulent flow being less inclined to separate.

1.3. The wall-near flow in this region of undoubtedly turbulent boundary layer has been visualized by a mixture of petroleum and magnesium carbonate; after evaporation of the petroleum, the magnesium carbonate shows, in white lines on the (black) wall of the ellipsoid, the integral curves of the directional field at the wall.

The results of these tests are represented *fig.* 1.1. — 1.3. :

1.3.1. *Fig. 1.1.* shows a side-view of the ellipsoid's rear part at $i = 10°$. The white lines clearly indicate a well-organized flow along the wall on flanks and underside of the obstacle, forming a system of well established wall streamlines, comparable in character with those in laminar flow.

On the upper side, an area of separated flow can easily be detected; it is delimited towards the "sound" (i.e. non-separated) flow over the flanks by a sharply drawn demarcation line.

Outside the separated area, even close to the demarcation line, the wall streamlines are only very little curved; moreover, they have obviously the direction of the flow outside the boundary layer.

The two hypotheses of §§ 1.1.1. and 1.1.2. are, therefore, clearly fulfilled, at least outside the separated area on the top of the ellipsoid.

1.3.2. *Fig. 1.2.* is a view of the separated area on the upper side of the rear of the body, seen from above.

The demarcation line (cf. § 1.3.1.) can be clearly observed; it separates the sound boundary layer with its very straight (turbulent) wall streamlines from an inner region with equally organized but much slower (and therefore probably laminar) flow.

Nevertheless, in this inner region too, wall streamlines can easily be detected. But, in conformity with [2], fig. 10.13. these (laminar) wall streamlines are considerably more swept than the turbulent ones. We shall return to this statement later on (§ 1.6.1.).

The streamlines themselves being indistinguishable from one another, we retain from this observation a practical criterion for regions of laminar or of turbulent flow : The sweep of the wall streamlines is considerably more important in zones with laminar flow.

We shall find, in § 1.6., not only further evidence confirming this criterion, but even an analytical explanation for the fact itself.

1.3.3. *Fig. 1.3* is a three-quarter view from behind on the line of demarcation between the separated area and the "sound" boundary layer. Except for a slight irregularity in the shape of the demarcation line (provoked by the supporting stem of the ellipsoid), this line proves to be a limit of wall streamlines from both sides and is therefore a wall streamline itself.

At its approach, the other wall streamlines become tangent to it, as they should; on the turbulent side, this takes place rather abruptly and only at the last moment — a phenomenon which can equally be observed in *fig.* 1.1.

1.4. It appears, from these experiments, to be beyond any doubt that wall streamlines not only exist in turbulent flow (hypothesis 2), but have — even more markedly than in the laminar case — the property of forming very small angles with the inviscid flow at the outer edge of the boundary layer, except for the immediate neighbourhood of a separated area on the obstacle under consideration (hypothesis 1).

1.4.1. This confirmation of the "principle of prevalence" in turbulent flow has an important consequence for the numerical determination of the form parameter of the turbulent boundary layer : We can apply, as in laminar flow (see [1], [3]), the principle of prevalence to "stream strips" (parts of the surface of an obstacle comprised between two neighbouring streamlines of the inviscid flow). These streamstrips are assimilable to bodies of revolution with a radius developing as the local distance e_2 of the constituting streamlines of the strip.

(*) Laboratoire de Mécanique des Fluides. The characteristics of this tunnel are :
Circular test section of 2.40 m length and 1.70 m diameter. The range of air speed varies from 28 m/s to 50 m/s; the degree of turbulence is $\frac{\sqrt{\frac{1}{3}(u'^2 + v'^2 + w'^2)}}{U_x} \sim 1\ \%$

1.4.1.1. The development of the momentum-loss thickness δ_2 of the turbulent boundary layer along such a streamstrip can then be calculated with the help of TRUCKENBRODT's well-known formula [7] for bodies of revolution :

$$\frac{\delta_2}{l} = \frac{\left[C_1 + \left(\frac{1}{2} c_{fl}\right)^{\frac{n+1}{n}} \int_{x_t/l}^{x/l} \left(\frac{U_e}{U_\infty}\right)^{3+\frac{2}{n}} \left(\frac{R}{R_0}\right)^{\frac{n+1}{n}} d\left(\frac{x}{l}\right)\right]^{\frac{n}{n+1}}}{\left(\frac{U_e}{U_\infty}\right)^3 \cdot \frac{R}{R_0}} \quad (*)$$

1.4.1.2. δ_2 once known by this expression, we can apply one of the semi-empirical formulas for the turbulent form parameter H, e.g. the formula of VON DOENHOFF and TETERVIN :

$$\delta_2 \frac{dH}{dx} = e^{4,080\,(H\ -\ 2,975)} \cdot \left[\ldots \frac{\delta_2}{q} \cdot \frac{dq}{dx} \cdot \frac{2q}{\tau_p} - 2,035\,(H - 1,286)\right]$$

with $q = \frac{\rho}{2} U_e^2$

In this formula, only τ_p (wall shear-stress) is still unknown; a first guess for it would be the formula of FALKNER :

$$\frac{\tau_p}{2q} = \frac{\alpha}{\left(\frac{U_e \cdot \delta_2}{\nu}\right)^{\frac{1}{n}}}$$

n is the same in TRUCKENBRODT's and in FALKNER's formula. For $n = 4$, we have $\alpha = 0{,}0128$; for $n = 6$, we have $\alpha = 0{,}0065$. Practically equivalent to FALKNER's formula is that of SQUIRE and YOUNG :

$$\frac{\tau_p}{2q} = \frac{0{,}0288}{\left[\log\left(4{,}075 \frac{U_e \cdot \delta_2}{\nu}\right)\right]^2}$$

1.4.1.3. Later on (§ 3.9.2.6.) we shall see that this proposed calculation of τ_p is too simple (and too much impregnated with two-dimensionality) to operate in cases with regions of very strong crossflow, as it occurs on ring airfoils.

In the case of ellipsoids at moderate incidences, the outcoming values of H are acceptable. Effectuated streamstrip by streamstrip, this computation then leads to a graduation of the whole surface of the obstacle with iso-H lines.

1.4.1.4. Two recent publications of J. P. JOHNSTON ([16], [17]) seem, however, to indicate that for obstacles with considerably skewed streamlines of the potential flow, this method is insufficient.

1.4.1.4.1. He develops, for skewed flow-configurations on plane surfaces, a method which is, at least in principle, more pertinent for these cases, but which does not immediately apply to curved surfaces; indeed, both the discussion of his work (cf [16]) as well as our own calculations show that such a generalisation must be made more carefully than indicated by JOHNSTON.

1.4.1.4.2. Nevertheless, the general idea of his work seems to explain at least a part of the difficulties mentioned in §§ 3.9.2.5. and 4.2. and will lead, by a felicitous application, to a pertinent definition of four parameters for the primary (H_1) and secondary (H_2) turbulent flow in three dimensions. This will be undertaken in a further study now under way.

1.4.1.4.3. In its present form, JOHNSTON's method cannot yet be employed for calculations on ring airfoils; we are therefore obliged, for a first analysis attempted here, to retain the generalisation of TRUCKENBRODT's formula sketched out above (§§ 1.4.1.1. and 1.4.1.2.).

1.4.2. In the laminar case, a similar application of POHLHAUSEN's method to the streamstrips (which are assimilated, as above, to bodies of revolution) led to a graduation of the surface in iso Λ lines (Λ = POHLHAUSEN's form parameter).

It thus became possible to write immediately a polynomial expression for the longitudinal flow :

$$\frac{u}{U_e} = \left(\frac{12 + \Lambda}{6}\right) \frac{n}{\delta} - \frac{\Lambda}{2} \cdot \left(\frac{n}{\delta}\right)^2 - \frac{4 - \Lambda}{2} \cdot \left(\frac{n}{\delta}\right)^3 + \frac{6 - \Lambda}{6} \cdot \left(\frac{n}{\delta}\right)^4$$

and another for the crossflow :

$$\frac{w}{U_e} = \frac{\delta^2}{6\,\mu U_e} \cdot \frac{\partial p}{\partial z} \cdot \left(1 - \frac{n}{\delta}\right)^3 \cdot \frac{n}{\delta}$$

where δ stands for the (local) boundary-layer thickness in laminar flow. With the help of these polynomials, one can write

$$\operatorname{cotg} \theta_p = \lim_{n \to 0} \frac{w}{u}$$

whence the formula of § 0.5.2.

1.4.3. It would therefore seem that an analogous computation should lead, in turbulent flow, to an expression of $\operatorname{cotg} \theta_p$ in terms of H.

Unfortunately, the general (power or logarithmic) laws for turbulent profiles, on which the definition of H is implicitly based, are not valid in the laminar sublayer.

Moreover, the crossflow profile in turbulent boundary layers is clearly not of power (nor logarithmic) character.

Thus, no analytical deduction of a $\operatorname{cotg} \theta_p$ formula for turbulent wall streamlines will, in a near future, be possible.

1.4.4. We are therefore obliged to make a reasonable hypothesis on the presumable form of the $\operatorname{cotg} \theta_p$ formula; the consequences of such a formula will be discussed and must be verified by experiment.

Such a reasonable hypothesis may spring from a careful analysis of the physical meaning of the laminar formula; the turbulent formula should then be built up in analogy to the laminar one.

1.5. To this effect, we write the laminar formula of § 0.5.2. in a slightly more general form :

$$\operatorname{cotg} \theta_p = c_L \cdot \frac{\Lambda - \Lambda_1}{\Lambda - \Lambda_2} \cdot \frac{\frac{\partial K_p}{\partial s} - c_1}{\frac{\partial K_p}{\partial z} - c_2}$$

1.5.1. It seems reasonable to suppose that the quotient

$$\frac{\frac{\partial K_p}{\partial s} - c_1}{\frac{\partial K_p}{\partial z} - c_2}$$

expressing (especially for $c_1 = c_2 = 0$ as in the ellipsoid case) the ratio of the longitudinal and transversal pressure gradients and therefore the influence of the potential flow outside the boundary layer on its stability *, has a

---

(*) $C_1 = \left\{\frac{1}{2} c_{fl}\left[\int_0^{x_t/l}\left(\frac{U_e}{U_\infty}\right) \cdot \left(\frac{R}{R_0}\right)^2 d\left(\frac{x}{l}\right)\right]^{\frac{1}{2}}\right\}^{\frac{n+1}{n}}$

c_{fl} = local wall-friction coefficient of the flat plate (c_{fl} in laminar, c_{fl} in turbulent flow)
x_t = transition point, R_0 = radius of reference.
In a streamstrip, we replace x by s and $R(x)$ by $e_2(s)$.

(*) EICHELBRENNER and MICHEL [8] have shown that the quotient $\frac{\partial p}{\partial s} / \frac{\partial p}{\partial z}$ plays a major rôle not only in problems of laminar separation, but also for that of transition to turbulent flow.

significance which is not restricted to laminar flow. We conserve, thus, this quotient as essential factor in the turbulent cotg θ_p formula.

1.5.2. The linear form $\Lambda - \Lambda_1$ plays, in laminar flow, an essential rôle for the separation in a symmetry plane :

Indeed, here θ_p must be either 0 or $\frac{\pi}{2}$; the second value has a physical meaning only at the separation point (in the symmetry plane) itself. Normally, we have thus cotg $\theta_p = \infty$, which corresponds to the fact that $c_2 = 0$ and $\frac{\partial K_p}{\partial z} \equiv 0$ for reasons of symmetry (cf. § 2.8. of the 1st Scientific Report).

1.5.2.1. In order to insure *at* the separation point a value $\theta_p = \frac{\pi}{2}$, the numerator of cotg θ_p must disappear, which normally * cannot be obtained by the expression $\frac{\partial K_p}{\partial s} - c_1$. Thus, $\Lambda - \Lambda_1$ has to disappear. Now, in two-dimensional or locally two-dimensional flow (as in a symmetry plane), we have $\Lambda = -12$. In order to make disappear $\Lambda - \Lambda_1$ at separation, we have to choose $\Lambda_1 = -12$.

1.5.2.2. Applying the same reasoning to the turbulent case, we should replace $\Lambda - \Lambda_1$ by a linear form $H - H_1$, where H_1 is the value of H at two-dimensional separation, i.e. $H_1 \sim 2$.

In § 3.9.2.7. will be discussed an objection against the hypothesis that in turbulent flow the symmetry plane always shows two-dimensional flow features. This may influence the value of H_1. Here we will admit this hypothesis without discussion.

1.5.3. A similar rôle is assumed by the linear form $\Lambda - \Lambda_2$ in the denominator : In the case of the ellipsoid, we have $c_1 = 0$. Moreover, there exists (cf. [4], *C* 2) a curve of absolute speed maximum on its surface having $\frac{\partial K_p}{\partial s} = 0$.

1.5.3.1. On such a line, no separation can take place; therefore $\theta_p \neq \frac{\pi}{2}$ and cotg $\theta_p \neq 0$. The vanishing numerator $\frac{\partial K_p}{\partial s} = 0$ must therefore be counterbalanced by a sufficiently strong zero of the denominator, whence $\Lambda - \Lambda_2 = 0$. Λ_2 must therefore be chosen as the value of Λ for a speed maximum in two-dimensional flow, i.e. as the form parameter of a flat plate. This gives $\Lambda_2 = 0$.

1.5.3.2. Once more, the same reasoning, applied to the turbulent case, provides $H_2 = 1{,}286$ (value for the flat plate corresponding to a power profile with $n = 7$).

We therefore replace $\Lambda - \Lambda_2$ by a linear form $H - H_2$ with $H_2 = 1{,}286$.

1.5.4. Finally, a "universal" factor c_T must be determined by experiment. This has been carried out by a comparison between wall streamlines computed with the formula

$$\text{cotg } \theta_p = c_T \cdot \frac{H - 2}{H - 1{,}286} \cdot \frac{\frac{\partial K_p}{\partial s} - c_1}{\frac{\partial K_p}{\partial z} - c_2}$$

at different c_T values and observations on ellipsoids (as in *fig.* 1.1 — 1.3) as well as on a ring airfoil of aspect ratio $\lambda = L/D = 1$, at $i = 15°$ incidence.

The second case has already been mentioned in the 2nd Quarterly Technical Report (figure 3; *fig.* 1.4 of this report). Comparison with *fig.* 1.5 (experimentally obtained configuration of wall streamlines) gives c_T between 0,5 and 0,7.

In a still unpublished thesis at Poitiers, Y. Grellier has checked these values in the case of the ellipsoid of revolution. He found, in fair agreement with the foregoing values, $c_T \sim 0{,}7$. This latter value will be adopted by us for all following considerations.

1.5.5. From the foregoing analysis, a formula

$$\text{cotg } \theta_p = 0{,}7 \cdot \frac{H - 2}{H - 1{,}286} \cdot \frac{\frac{\partial K_p}{\partial s} - c_1}{\frac{\partial K_p}{\partial z} - c_2}$$

seems to be the most promising generalization of the laminar expression of § 0.5.2. for wall streamlines.

As in the laminar case, we have $c_2 = 0$ for obstacles with a symmetry plane, whereas c_1 depends on the kind of obstacle chosen.

For ellipsoids we have, in virtue of the considerations of § 1.5.3., $c_1 = 0$.

In the case of ring airfoils, which we shall analyze later on, we find $c_1 \neq 0$. The value of c_1 depends, in this case, on the aspect ratio, the incidence and (probably) the Reynolds number.

1.6. The proposed formula of § 1.5.5. can be checked by another comparison: That of the already mentioned (§ 1.3.2.) difference between laminar and turbulent wall streamlines.

1.6.1. Indeed, in all observed cases, the laminar wall streamlines appear considerably more swept than the turbulent ones.

Now, the domain of variation of H is not only restricted to the narrow interval $1{,}1 < H < 2$, but it is moreover well known (cf. also [2], chapter xxii, *b* 3), as follows — see *fig. 1.6* — from Von Doenhoff and Tetervin's formula, that $H \sim 1{,}4$ until immediately before separation. Thus, $0{,}7 \cdot H\text{-}2/H\text{-}1{,}286 \sim -4$.

On the contrary, Λ has a much wider domain of variation, $+12 > \Lambda > -12$, and drops (without regions of nearly constant value) rapidly towards -12. Thus $-\infty < \frac{\Lambda + 12}{\Lambda} < 0$ with rapid variation for $0 > \Lambda > -12$.

1.6.2. In the turbulent case, cotg θ_p is thus over the greatest portion of the non-separated flow region nearly constant and (absolutely) very great; θ_p is therefore small and the corresponding wall streamline straight and nearly parallel to the outer flow.

In the laminar case, cotg θ_p continuously varies from (absolutely) great values to very small values; θ_p thus undergoes a great variation long before separation : The laminar streamlines are much more swept than the turbulent ones.

1.6.3. This result agrees very well with the observations and, in particular, with *fig. 1,1* on the one side and fig. 10,13 of [2] on the other side.

It constitutes, therefore, a fair confirmation of the proposed formula.

(*) In the case of the ellipsoid we have, cf. [1], $c_1 = 0$ and $\frac{\partial K_p}{\partial s} \neq 0$ at separation!

2. Separation and Reattachment in Turbulent Flow

2.0. In the Introduction (§ 0.4.) we mentioned one of the most important results of the laminar boundary-layer theory in three dimensions, the definition of the three-dimensional separation line as a singular wall streamline (limit of an infinity of regular wall streamlines) passing through a point of divergence (separation point, admitting at least two wall streamlines instead of one).

2.0.1. The further considerations (in particular § 1.0.) make it obvious that the main mechanism of separation will be the same in turbulent flow. A mathematically and physically reasonable definition of the three-dimensional separation line in turbulent flow over a (predominantly convex) body seems therefore to be the following:

2.0.2. The (turbulent) separation line on a (convex) finite body is a singular wall streamline (limit of regular wall streamlines in turbulent flow) passing through a point of divergence. Such a point is defined by the (only necessary) condition $\left(\frac{\partial \vec{V}}{\partial n}\right)_p = 0$ which in presence of a plane of symmetry on the obstacle ($c_2 = 0$) is equivalent — as in laminar flow — to the double condition $\frac{\partial p}{\partial z} = 0$ and $H = 2$.

2.0.3. Once the potential flow over the obstacle known and a graduation in H of the surface established by the procedure of § 1.4.1., the intersection of the two (linear) systems $\frac{\partial p}{\partial z} = 0$ and $H = 2$ defines a (normally, i.e. in all non-degenerated * cases) finite number of points with $\left(\frac{\partial \vec{V}}{\partial n}\right)_p = 0$.

It is, therefore, easily possible to discern, by consideration of the wall-streamline configuration in the neighbourhood of this finite number of points, the points of divergence from other singular points (e.g. those of convergence).

2.0.4. Beginning in such a point, the singular wall streamline (characterized by an angle $\theta_p \sim \frac{\pi}{2}$ in this point) can be calculated, step-by-step, with the help of the turbulent analogue to Oudart's formula (see § 1.5.5.) :

$$\operatorname{cotg} \theta_p = 0{,}7 \cdot \frac{H - 2}{H - 1{,}286} \cdot \frac{\frac{\partial K_p}{\partial s} - c_1}{\frac{\partial K_p}{\partial z} - c_2}$$

In the case of ellipsoids, which we consider first, we have $c_1 = c_2 = 0$.

2.0.5. The numerical calculation of this line, in the case of an ellipsoid of revolution, with an incidence $i = 10°$, is under way at Poitiers (part of a still pending thesis). Experimental results of this case are already available and are shown in *fig. 1.1 — 1.3.*

2.1. We find, indeed, in these pictures not only a good confirmation of the concept of wall streamlines in general (§ 1.3.), but moreover (cf. [9]) an experimental proof of the validity of the above definition of the separation line:

2.1.1. All three pictures show, beyond any doubt, a demarcation line between an outer region ("sound" boundary layer) of turbulent character * and an inner region ("separated area") of laminar flow (considerably more swept wall streamlines).

2.1.2. This demarcation line is obviously a limiting curve of the wall streamlines of the outer (turbulent) region and therefore itself a (singular) wall streamline. On the other hand, this line is the frontier of the inner area with separated flow towards the sound flow, and therefore the separation line in the sense of § 0.4.

2.1.3. The identity of the line of separation in three-dimensional turbulent flow and of the singular turbulent wall streamline formed as a limit of an infinity of regular wall streamlines is, therefore, experimentally established in a very satisfactory manner.

2.2. *Fig. 2.1* shows schematically the configuration of turbulent wall streamlines near the symmetry plane of an obstacle at the approach of a separated area. This part of the flow cannot be seen on the *fig. 1.1 — 1.3*; indeed, for the test Reynolds number of $\sim 6.10^6$, the laminar separation on the upper side of the ellipsoid takes place, according to [8], *upstream* from the transition line: transition occurs earlier than separation only on the flanks and on the underside.

Nevertheless, the visualisation of such a configuration has been possible in another case, see *fig. D1 — D3.*

2.2.1. We will occasionally call (in a mathematically improper, but short expression) the limiting line of separation a "forward envelope" of turbulent wall streamlines. This denomination will only reveal its full meaning later (§ 2.4.5.). For the moment, it describes very well the movement of deviation in the wall-near boundary layer when the viscous flow tries to avoid a region of unfavorable pressure distribution on the obstacle.

2.2.2. The separation point on the line of symmetry is the intersection (see § 2.0.3.) of $\frac{\partial p}{\partial z} = 0$ and $H = 2$; in the two-dimensional case, where $\frac{\partial p}{\partial z} \equiv 0$, the condition degenerates and the separation points form a line which coincides with the line $H = 2$. This is the two-dimensional separation "line", an infinite repetition of identical separation points, as it should be. The two-dimensional sepa-

(*) Only in intrinsically two-dimensional cases (bodies of revolution without incidence, yawed infinite cylinders etc.), do we find an *infinite* number of such points which are, however, equivalent to each another.

(*) The region is located downstream the transition line (calculated in [8]) for the Reynolds number 6.10^6 in question; moreover, the straightness of the wall streamlines indicates (cf. § 1.3.2.) turbulent flow.

ration is thus recognized as a particular case of three-dimensional separation, as in laminar flow (cf [3]).

2.3. In this two-dimensional (turbulent) case, there exists a complementary configuration to that of separation: The reattachment.

2.3.1. On principle, reattachment can be observed, too, in laminar flow; however, laminar reattachment plays a minor rôle and will be, for the moment, left aside; later on, we shall find a particular case of laminar reattachment in three dimensions which will be treated in § 3.11.

2.3.2. Reattachment supposes, as the name implies, a foregoing separation, occurring in general near the leading edge of a profile with incidence, in particular when this leading edge has a small radius of curvature. We then find a high negative pressure peak immediately behind the leading edge, which is followed by a steep unfavorable pressure gradient that the (generally laminar) boundary layer cannot stand.

A subsequent interval of nearly uniform pressure favors the reattachment of the separated layer which is generally preceded (or at least accompanied) by transition in the layer, indicated on the pressure curve of *fig. 3.19* by a short level in the steep rise, see § 3.10.2.2.

2.4. One of the simplest three-dimensional cases of reattachment of this kind can be observed on the upper (outer) side of a ring airfoil with incidence.

2.4.1. As already mentioned (§ 0.7.), the first experimental observations were made, incidentally, in the course of an investigation on leading edge adaptation, carried out 1959 by BTZ [5].

2.4.2. In the case represented *fig. 1.5* ($\Lambda = 1$, profile NACA 66-006, $i = 15°$), the pressure distribution on the upper side (calculated according to WEISSINGER [10], cf. § 3.1.), has been checked in the windtunnel of ISL *. The result is represented in *fig. 3.5* :

A negative pressure peak at the leading edge is followed by a steep pressure rise which causes immediate separation. This separation is, however, limited to the upper half of the outer side, the pressure peak on the lower half of the ring airfoil being located on its *inner* side.

2.4.3. In *fig. 1.5*, this separation line, nearly parallel to the leading edge, can be seen particularly well. Even the well-known pattern of wall streamlines at the approach of laminar separation, as sketched in *fig. 2.2*, can easily be found inside the narrow strip of non-separated flow between leading edge and pressure minimum.

2.4.4. On the other hand, the flow pattern near the trailing edge shows a well-attached "sound" turbulent boundary layer. The fact that this layer is really turbulent, has been confirmed by the considerations of [11]; we will not dwell upon it here.

Between the (laminar) separation at the leading edge and the region of sound (turbulent) flow near the trailing edge, there must necessarily take place a turbulent reattachment along a line of momentarily unknown character.

2.4.5. However, we know one thing: This line must form the limit between the separated area behind the leading edge and the sound turbulent boundary layer farther downstream.

2.4.5.1. Such a limiting line can indeed be found on *fig. 1.5:* The separated area of roughly heart-shaped form and organized flow in its interior is separated, by a sharply determined demarcation line, from the sound boundary layer.

2.4.5.2. The wall streamlines (visualized by a mixture of petroleum and lamp black on a dull-white surface) in the region of sound flow can easily be followed upstream.

They are straight until very close to the heart-shaped separated area, where they bend rather suddenly to form a well-marked limit.

2.4.5.3. This limit, which will be called for the sake of brevity (in a mathematically improper expression, analogous to that of § 2.2.1.) a "rearward envelope" of wall streamlines, is a (singular) wall streamline itself.

The whole configuration is obviously the inverse of turbulent separation; indeed, the flow pattern of *fig. 1.5* could as well be "read" in the opposite sense and would then constitute a remarkably well-designed separation picture.

2.4.5.4. The singular wall streamline, locally indistinguishable from other wall streamlines, can only be characterized by the fact of passing through (at least) one point of ramification on the surface. This point has the character of an inverse point of divergence ("negative separation point" or "point of reattachment") and is located, in the case of *fig. 1.5*, in the plane of symmetry on the upper side. Its configuration is sketched in *fig. 2.3.*

2.4.5.5. We call this singular wall streamline a "reattachment line"; it is the natural generalization of the two-dimensional reattachment and — as such — the inverse of separation.

2.5. From all this, we can draw the following definition :

The reattachment line in turbulent flow is the rearward envelope of an infinity of (regular) wall streamlines and therefore a (singular) wall streamline itself.

It passes through a point of reattachment (necessary condition: $\left(\frac{\partial \vec{V}}{\partial n}\right)_p = 0$) on the surface of an obstacle and can be obtained by a step-by-step integration of the formula for $\operatorname{cotg} \vartheta_p$ in § 2.0.4.

2.6. Nearly all figures of the picture series *A*, *B* and *C* show, under various conditions to be analyzed later, the conclusiveness of the above definition.

2.6.1. The real problem is, in general, the determination of the reattachment point, from which the determination of a reattachment line should start.

2.6.2. We discuss this question, in the following paragraph, for the particular case of an obstacle having a plane of symmetry parallel to the general direction of flow; this plane is represented, on the surface of the obstacle, by a symmetry *line*.

We already know that in this case $c_z = 0$.

2.7. The reattachment line must form, by virtue of our definition in § 2.5., an angle $\vartheta_p = \frac{\pi}{2}$ with the symmetry line on the surface. Thus, $\operatorname{cotg} \vartheta_p$ must be equal to zero in the corresponding reattachment point, i.e. the nominator of the $\operatorname{cotg} \vartheta_p$ formula must vanish.

2.7.1. We therefore find either $H = 2$ or $\frac{\partial K_p}{\partial s} = c_1$.

(*) "Institut Franco-Allemand de Recherches Scientifiques", St-Louis, Haut-Rhin, France. The tunnel is of Prandtl-type, see [5].

Now, $H = 2$ is characteristic for a trailing-edge separation and therefore excluded in the reattachment point which is by necessity located upstream the (turbulent) separation near the trailing edge.

2.7.2. The condition for reattachment in the symmetry plane is thus given, necessarily, by $\frac{\partial K_g}{\partial s} = c_1$. The problem of determination of the reattachment point is thus transformed into that of finding c_1.

2.8. We already know that c_1 depends on the geometrical and aerodynamical configuration of the obstacle, i.e. on its form and incidence, possibly too on the Reynolds number.

But no general statement can be made except that the choice of c_1 must ensure the "unicity" of the reattachment point. We shall see that this condition is indeed sufficient in the case of ring airfoils, which will be treated in the following chapter; cf. too the 1st Scientific Report.
2.9. A short, but exhaustive survey of the problems treated in this chapter may be found in a recent French publication of the author [12]. In particular, the location and interpretation of the leading-edge separation has been amply discussed in this paper, so that we do not need to insist here on this particular point, which has also been mentioned in the 3rd Quarterly Report.

3. Separation and Reattachment on Ring Airfoils

3.0. As already mentioned (§ 2.4.), one of the simplest cases where three-dimensional leading-edge separation occurs is that of a ring airfoil at incidence, having a profile with sharp nose radius.

3.0.1. Such a profile, chosen in former investigations [5], is the symmetric laminar profile NACA 66-006.

All ring airfoils in the following considerations and tests have therefore been equipped with this profile, in order to reduce the work of computation and to facilitate comparisons with previous results.

3.0.2. Ring airfoils have, in addition to their simplicity of configuration and construction, the advantage of permitting a reliable theoretical calculation of the inviscid flow around and through them. Indeed, WEISSINGER developed a computation method [10] which seems to give good results even up to considerable incidences (cf. [5]).

3.0.3. According to an (arbitrary, but for all practical purposes accepted) definition *, cylindrical ducts are considered as "ring airfoils" only for $\lambda = L/D < 2$.

On the other hand, we are interested, for purposes of comparison with plane wings, in the behavior of the flow for $\lambda \longrightarrow 0$.

This (and questions of rapid convergence of the WEISSINGER method) leads to the restriction of our investigations to ring airfoils with $0 < \lambda < 2$.

3.0.4. As representative cases were chosen those of ring airfoils with $\lambda = 1$, $\lambda = 0{,}5$ and $\lambda = 0{,}2$.

For these cases, with NACA 66-006 profiles, the inviscid flow over the (outer) upper surface of the airfoil has been computed, for a certain number of (not too great **) incidences, by WEISSINGER's method:

3.1. Brief Outline of the WEISSINGER Method (see [5]).

3.1.1. In a series of studies and reports, J. WEISSINGER developes a theory of linearized treatment for the calculation of the aerodynamic coefficients of annular wings.

3.1.2. The linearization permits a separation of form — and thickness — effects, the first ones being attached to the distribution of center lines around the annular wing, the second ones to the local thickness of the airfoil.

In accordance with the linear theory, all the limiting and boundary conditions of the problem, as well in the case of form — as in the case of thickness — effects, are localized on a basic (straight circular) cylinder of radius R chosen as an (optimum) approximation of the real configuration and placed parallel to the air flow at infinity.

3.1.3. This latter condition is maintained even in the case of an inclined straight cylinder. A careful distinction must, therefore, be made between this "basic cylinder" having its axis always parallel to the flow, and the real wing of may-be cylindrical form (*fig. 3.1* shows the coordinates applied in WEISSINGER's [5] calculation method).

(*) Established by the US Patent Office.

(**) Limited to incidences $i < i_{crit}$, where i_{crit} is the critical incidence for stalled flow on the upper surface; the list of incidences in function of λ is given in *table 3.1*.

3.1.4. The effects of the outer line distribution, for an infinitely thin wing, are calculated by means of decomposition in double FOURIER series, of the profile form as well as of the distribution of the circulation on the basic cylinder.

3.1.5. *Fig. 3.2* shows the profile-thickness distribution with the calculated distribution of $t(\xi) = \sum_{j=1}^{6} t_j \sin j\,\vartheta$ (see [5], § 1.1.3.2.) on the one hand, and that of the NACA 66-006 profile, on the other hand.

The two curves agree very well one with another.

3.1.6. In WEISSINGER's method, the occurring *axial velocity* represents the result of a linear superposition of three induced speeds with the axial component of the free-stream velocity.

3.1.6.1. The induced speeds are the following ones :

$\frac{v_{xq}}{U_\infty}$ induced by the (thickness-) source distribution

$\frac{v_{x0}}{U_\infty}$ produced by the thickness-induced vortex distribution

$\frac{v_{x1}}{U_\infty}$ induced by the incidence-generated vortex distribution.

3.1.6.2. By linear combination of the velocities, we obtain the final result :

$$\frac{v_x}{U_\infty} = \cos i + \frac{v_{xq}}{U_\infty} + \frac{v_{x0}}{U_\infty} + \frac{v_{x1}}{U_\infty \cdot \cos\varphi} \cdot \cos\varphi$$

3.1.7. For the calculation of the *circumferential velocity*, WEISSINGER (ref. [10]) found the following results:

The total circumferential velocity v_φ at the surface is the combination of the circumferential mainstream component $i \cdot U_\infty \cdot \sin\varphi$ of the mean induced velocity $v_{\varphi 1}$ and of the non-continuous term of opposite signs on both sides of the surface, the absolute value of which being that of the axial vorticity.

$$v_\varphi = U_\infty \cdot \sin\varphi \left\{ i \pm \frac{\lambda}{2} \cdot \int_{-1}^{\xi} g(\xi')\, d\xi' \right\} + \bar{v}_{\varphi_1}$$

with the sign + for the outer side of the wing surface and the sign — for the inner side of the wing surface.

3.1.8. *Tables A1 — A3* * give for the different λ the results which permit the determination of the different elementary velocities:

$$\frac{v_{xq}}{U_\infty},\ \frac{v_{x0}}{U_\infty},\ \frac{v_{x1}}{U_\infty \cos\varphi},\ \frac{v_\varphi}{U_\infty \sin\varphi}$$

3.1.8.1. Once the velocities $\frac{v_x}{U_\infty}$ and $\frac{v_\varphi}{U_\infty}$ are known, one can design the velocity field which gives, by integration, the streamlines of the potential flow of the airfoil.

3.1.8.2. *Tables A2 and A3* correspond to a constant distribution of local incidence, i.e. to a straight profile-center line.

For the calculation, we put $i_1^{(0)}(\xi) = 1$ ([5] § 1.1.1.1.)

(*) See remark in the Annex.

3.1.9. The axial velocities $\frac{v_x}{U_\infty}$ and circumferential velocities $\frac{v_\varphi}{U_\infty}$ for the different λ and incidences have been employed for computation of the pressure coefficient K_p, after BERNOULLI.

$$\left(\frac{U_e}{U_\infty}\right)^2 = \left(\frac{v_x}{U_\infty}\right)^2 + \left(\frac{v_\varphi}{U_\infty}\right)^2$$

$$K_p = 1 - \left(\frac{U_e}{U_\infty}\right)^2$$

3.1.10. *Fig. 3.3 — 3.7* show the distribution of K_p in function of ξ for $\varphi = 180°$, for a ring airfoil with $\lambda = 1$ and incidences $i = 0°$, $i = 9°$, $i = 15°$, $i = 18°$ and $i = 21°$.

K_p is plotted against the pressure coefficients measured in ST-LOUIS (see [5] § 2.4.2.).

Up to an angle of incidence $i = 15°$ the pressure coefficients calculated here coincide quite well with measured ones, whereas for $i = 18°$ and $i = 21°$ the difference between the results shows more important.

3.1.11. *Fig. 3.8 — 3.10* represent the velocity distribution $\frac{U_e}{U_\infty}$ in function of s for different streamstrips. s is the mean direction in each streamstrip (see § 1.4.1.) of the outer (upper) part of the airfoil. As examples for different ring airfoils we have given:

for $\lambda = 1$ the velocity distribution for $i = 15°$
for $\lambda = 0{,}5$ that of $i = 9°$
and for $\lambda = 0{,}2$ that of $i = 6°$.

Thus, we have furnished three examples which remain on the safe side of the beginning stall of the airfoil and which, therefore, give a certain presumption that WEISSINGER's theory mat still apply.

3.1.12. *Tables A4 — A15** show K_p calculated with WEISSINGER's method [10] for the different ring airfoils with incidence (see § 3.0.4.).

3.2. The corresponding tests in the windtunnel at POITIERS (characteristics of the tunnel see § 1.2.) have been executed on three models with profiles NACA 66-006:

3.2.1. Wooden model of $\lambda = 0{,}2$ with $L = 0{,}2$ m and $D = 1$ m, as represented by *fig. 3.11*. Its dimensions have been chosen in function of the diameter of the test section of the tunnel, in order to reduce the wall influence to a minimum:

3.2.1.1. The complete velocity field outside a ringfoil of $\lambda = 0{,}2$ and of profile NACA 66-006 has been calculated *(fig. 3.12)*, according to WEISSINGER, for a maximal incidence of $\sim 20°$ envisaged **.

The ratio of airfoil and test-section diameters has been fixed so as to ensure a maximum deviation between streamlines and tunnel wall of 5%, where account is already taken of the boundary layer displacement-thickness of tunnel and model.

3.2.1.2. To avoid deformations of the (not very rigid and — see *fig. 3.13* — heavily loaded) model, its fixation in the tunnel is made (instead of strings as in the case of the model for $\lambda = 1$, see § 3.2.3. below) by means of a profiled bar, traversing horizontally tunnel and model. Its influence on the flow at the upper (outer) part of the model surface, where all observations will be carried out, is negligible; on the other hand, this means of fixation permits — apart from stiffening the model — a very convenient determination of the model's incidence *.

3.2.2. Wooden model of $\lambda = 0{,}5$ with $L = 0{,}3$ m and $D = 0{,}6$ m (see *fig. 3.14*). The same kind of fixation as for the preceding model has been utilized.

3.2.3. The model $\lambda = 1$ made of electron has been chosen in the following dimensions : $L = D = 0{,}40$ m (see *fig. 3.15*). The pressure distribution along the profile of the annular wing has been obtained by means of 21 pickups (1 mm interior diameter, 2 mm exterior diameter) connected to the water columns of a multimanometer; 10 pickups on the exterior surface, 10 on the inner surface and 1 pickup at the leading edge, which latter gives the total pressure. The pressure tubes were lodged in milled slots which were, afterwards, filled up with Araldit to reconstitute a smooth wing surface.

3.2.3.1. The ST-LOUIS' tests have been executed not only in order to obtain visualisations of the boundary layer, but also measurements of the aerodynamical forces. The model was therefore hung up by means of steel wires and thus controlled by contact and by means of an electrical motor the beam movements of an electromechanical 6 components-balance.

3.2.3.2. The POITIERS' tests having been restricted to visualisations of the boundary layer, it was possible to fix the model in the same simple and practical manner as the models $\lambda = 0{,}2$ and $\lambda = 0{,}5$, i.e. by means of a profiled transversal bar (see e.g. *fig. C 6*) permitting quick determinations of the test incidences.

3.3. All models have been painted in dull-white (to avoid reflections of light, especially with flash photos); different kinds of ointment (mixtures of petroleum and lampblack, talc or magnesium carbonate) have been tried, on the viewpoint of photography as well as on that of visualisation strictly speaking.

Best results have been obtained with an ointment composed of a mixture of petrol and lampblack. All pictures of the series A, B, C and D have been taken in this way.

3.4. The tests carried out at the ISL in 1959, and those performed at POITIERS, have shown different values of incidence for identical flow configurations on the airfoil $\lambda = 1$.

3.4.1. This can be explained by the fact that the two windtunnels are of different type:

The windtunnel at ST-LOUIS presents (cf. [5]) a free vein without noticeable effect of the walls, whereas the windtunnel at POITIERS (§ 1.2.) has a guided vein.

3.4.2. For a guided vein, the induced speed corresponds to an increase of incidence, whereas, for a frec vein, it means diminution of incidence. At similar lift, if i_g is the geometrical incidence for a guided vein, one can write for a free vein

$$i = i_g - \Delta i$$

Δi, which has a value of about 3° for high incidences (21° at POITIERS correspond to 18° at ST-LOUIS) becomes zero for axial flow ($i = 0$). *Fig. 3.16* gives the variation of Δi in function of the angle of incidence of a ring airfoil in the guided vein.

(*) See remark in the Annex.
(**) In reality, only incidences of about 10° proved necessary; indeed, complete stall occurred already at $\sim 9.5°$, cf. *fig. C7 — C9* and *table 3.1*.

(*) For the difference between geometrical and aerodynamical incidence in different types of tunnels (PRANDTL and EIFFEL type), see § 3.4.

3.5. The influence of the Reynolds number on the different "constants" in the cotg θ_s formula being still unknown, it seemed essential to perform all tests at comparable Reynolds numbers $\mathcal{R}_L = \frac{LU_\infty}{\nu}$.

3.5.1. The range of tunnelspeeds at POITIERS being limited between 28 m/s and 50 m/s (cf. § 1.2.), the tests on the ($\lambda = 1$) — model had to be executed at 28 m/s, those on the ($\lambda = 0{,}5$) — model at 37 m/s and those on the ($\lambda = 0{,}2$) — model at 45 m/s.

3.5.2. The two cases $\lambda = 1$ and $\lambda = 0{,}5$ thus show the same Reynolds number of about $0{,}8 \cdot 10^6$; in the case $\lambda = 0{,}2$ the upper limit of the tunnelspeed permitted only a number of $\mathcal{R}_L = 0{,}65 \cdot 10^6$, but always of the same order.

3.6. After each test, photos were taken to show the final * pattern of the visualized wall streamlines. The results can be seen in *fig. A 1 — A 8, B 1 — B 12, C 1 — C 12.*

Only the picture *C 12* has been obtained in a different manner: To show the beginning of the flow organization on the back of the airfoil, a flash of the starting configuration has been taken.

3.7. For $\lambda = 0$, results from an unpublished ONERA test series (executed at CANNES on plane wings between panels) were available. These wings had sharp leading edges and showed different profiles. Separation and stall were determined by means of tuft studies and with the help of smoke issued from slots in the surface.

3.7.1. The results, therefore, were less accurate than those of the very carefully executed tests of POITIERS. They gave critical incidences varying, for the different profiles, between $i_{crit} = 5°$ and $i_{crit} = 7°$.

3.7.2. Nevertheless, these results permit an (at least) qualitative control of the extrapolation of the test results, obtained at POITIERS, towards $\lambda = 0$. This has been done (cf. § 3.10.3. and *fig. 3.28*) and leads to a satisfactory agreement.

3.8. From the photos (A1 — A10, B1 — B12, C1 — C12), one can easily see that in all cases and for all incidences (below the critical one, defined by the contact between the separated areas on the upper side of the airfoil, cf. § 3.0.4), the flow configuration is — at least in principle — the same, corresponding to that sketched in *fig. 3.17*:

3.8.1. Close to the leading edge, and — broadly speaking — approximately parallel to it, a (probably laminar) separation of the boundary layer takes place over about 180° leading-edge perimeter (upper half of the outside of the ring airfoil). Behind this separation line is located an approximately heart-shaped separated area ("bubble") with organized flow in its interior; tuft studies ** have shown that its thickness is very small, so that the shear layer between this separated area and the potential flow over the upper side of the airfoil remains very close to the wall, cf. *fig. 3.17*. In first approximation, the shearlayer may therefore be assimilated to a (turbulent) boundary layer, transition occurring in it generally (see § 3.11 for an exception) before reattachment.

3.8.2. The downstream limit of the bubble is a reattachment line in the sense of § 2.4. and 2.5., followed by an ordinary turbulent boundary layer.

For small angles of incidence, this ordinary turbulent boundary layer shows no trailing-edge separation; for larger angles of incidence, a trailing-edge separation, as indicated in *fig. 3.18.*, makes its appearance.

(*) i.e. after evaporation of the petroleum.

(**) Made in 1959 at the ISL.; a new and more systematic series of tests is under way, at present, in the "Laboratoire de Mécanique des Fluides" at POITIERS (France).

3.8.2.1. Spreading progressively, it comes into contact with the bubble ("critical" incidence, $i = i_{crit}$), creating thus a corridor of reflux over the whole upper side of the airfoil ("stalled" flow, see *fig. 3.20*).

Two strong shearlines separate the flow in this corridor from the not separated viscous flow over the flanks. At the forward points of these shearlines, two strong vortices are forming which can be seen in *fig. C9 — C12*; cf. too [11], fig. 5.

3.8.2.2. Corridor and vortices bring about a strong perturbation of the potential flow, so that — contrary to the interval $i < i_{crit}$ — the WEISSINGER method gives here no longer trustworthy results. A hope of theoretical determination of the viscous flow configuration exists, therefore, only for incidences up to the critical incidence; this hope is still further restricted by the remarks in § 3.10.2.2.

3.8.3. As the *fig. 3.3 — 3.7* and the considerations of § 2.4.2. show, a close relation exists between the pressure distribution over the airfoil and the configuration as sketched in *fig. 3.18*. This relation is illustrated by *fig. 3.19*. With the help of WEISSINGER's method, this relation can be easily established, at least, in the symmetry plane of the ring airfoil, as long as $i < i_{crit}$.

This gives the (approximate) position of the points of (laminar) separation at the leading edge, of (turbulent) reattachment and, finally, of the (turbulent) trailing-edge separation on the upper side of the ring airfoil.

3.8.4. The development of the configuration here above described has been very carefully analyzed, in the EIFFEL windtunnel at POITIERS, for $\lambda = 0{,}2$; 0,5 and 1 (see *photos A1 — A8, B1 — B12, C1 — C12* and *D1 — D3*).

3.8.4.1. The results of this analysis have been reported in *tables 3.2* (1. and 2.), *3.3* (1. and 2.), *3.4* (1., 2. and 3.) as well as in *fig. 3.21, 3.22* and *3.23*.

It can be seen that the trailing-edge separation is very difficult to observe; only for $\lambda = 1$, could pictures yielding evidence *(D1 — D3)* be taken: the results can be found in *table 3.4.3.*

In all other cases, a strong presumption subsists, that the trailing-edge separation starts immediately before the leading-edge bubble reaches the trailing edge, but no full proof could be obtained on these wings of insufficient depth; cf. the remarks in the 2nd Scientific Report (§§ 1.3. and 2.2.).

3.8.4.2. In the following considerations, we shall make this assumption, clearly demonstrated for $\lambda = 1$, strongly suggested for $\lambda = 0{,}5$ and $\lambda = 0{,}2$: We shall suppose that the contact between leading-edge bubble and trailing-edge separation is established immediately *before* the bubble reaches the trailing edge, where the trailing-edge separation had just had the time to start.

3.8.4.3. In particular, it therefore seems reasonable to assume for $\varphi = 180°$ (i.e. at the symmetry line on the upper side of the airfoil), that $H = 2$ at the trailing-edge just before $i = i_{crit}$.

3.8.5. A very important conclusion on the character of the reattachment (turbulent or laminar) will be drawn from the flow pictures of the series A — C in a following paragraph (§ 3.11.); for the moment, we will consider the whole reattachment as turbulent and try, with this assumption, a numerical computation of the reattachment line in the best established case of the three ($\lambda = 1$).

3.9. This computation has been executed for the three incidences $i = 9°$, $i = 15°$ and $i = 18°$ (incidences in terms

of the open test-section tunnel of the ISL at St-Louis; the corresponding incidences in the Eiffel tunnel at Poitiers are — cf. *fig. 3.16* — $i_e \sim 10\frac{1}{2}°$, $i_e \sim 17°$ and $i_e \sim 21°$).

3.9.1. The case $i = 9°$ (cf. *C1*) shows a very small and scarcely developed leading-edge bubble, practically no sweep of the wall streamlines in the non-separated boundary layer and no trace at all of any trailing-edge separation.

The graphs relative to this case have been presented in the 1st Scientific Report; the results are of no particular interest and will not be reproduced here.

3.9.2. The case $i = 15°$ (*fig. 1.5* and *C2*) presents a considerably greater interest; it will be treated in extenso hereafter:

3.9.2.1. Weissinger's method (see § 3.1.) permits a complete calculation of the pressure distribution on the upper (outer) surface of the airfoil and thus a determination of the directional field of the inviscid flow on this surface, as represented by the numerical *tables A11-A13.*

The integration of this directional field yields the potential streamlines and, consequently, the determination of the *s*-coordinate directions. The corresponding directions of the *z*-coordinate are the orthogonal trajectories of the foregoing.

Graph I represents the streamlines of the outer flow (potential streamlines at the wall) between $\varphi = 90°$ and $\varphi = 180°$ as measured, from 11,25° to 11,25°, on the leading edge.

The streamstrips, as defined in § 1.4.1., have been delimited by each two of these streamlines having an angular distance of $22\frac{1}{2}°$ (and therefore overlapping one another). All characteristic values in these streamstrips (δ_2, H, etc.) have been associated to their "middle line" at angular distance of 11 1/4° from each boundary.

3.9.2.2. The knowledge of the entire pressure distribution and of the network of curvilinear coordinates (s, z) then permits the determination of $\frac{\partial K_p}{\partial s}$ and of $\frac{\partial K_p}{\partial z}$ over the whole concerned portion (i.e. the upper half of the outside) of the surface. The resulting iso-$\frac{\partial K_p}{\partial s}$ and iso-$\frac{\partial K_p}{\partial z}$ lines are represented in *Graph I.*

It is therefore possible to apply, streamstrip after streamstrip, Truckenbrodt's formula (§ 1.4.1.1.) for δ_2.

3.9.2.3. Here a problem arises: How should we treat the shear layer above the separated area of the bubble, and where should we assum the transition of shear or of boundary layer from laminar to turbulent flow? Even in two-dimensional theory, no pertinent information is available; in three dimensions, only more or less reasonable hypotheses can be made. It was therefore decided to consider — in the absence of other information and for the sake of simplicity — the shear layer as in first approximation equivalent to a turbulent boundary layer whose outer velocity distribution is given by the results (§ 3.9.2.1.) obtained according to Weissinger.

No attempt has been made to calculate the laminar boundary layer between leading edge and leading-edge separation, by reason of the inexactness such a calculation would necessarily suffer from the extraordinarily strong crossflow.

On the other hand, the initial conditions play, in all boundary-layer calculations, only a second-order rôle for the features sufficiently far downstream; so it was considered as exact enough to begin the calculations according to Truckenbrodt, in each streamstrip, with $\delta_2 = 0$ at a conventional position. As such a conventional beginning was chosen the parallel to the leading edge through the (laminar) separation point on the wing's symmetry line ($\varphi = 180°$).

The results thus obtained for δ_2 are contained in the numerical *tables A16 — A21.*

3.9.2.4. With these values of the outer flow and of δ_2, the formula of Von Doenhoff and Tetervin for dH/dx, together with Squire and Young's formula for τ_p (§ 1.4.1.2.), permits the determination of H in the whole region.

As initial value of H, corresponding to $\delta_2 = 0$, has been assumed $H = 1{,}286$; a variation of this value within relatively large limits ($1{,}286 \leqslant H \leqslant 1{,}4$) had only a very small influence on the final results.

3.9.2.5. This computation should give, on the symmetry line (quasi two-dimensional streamstrip) a final value of H (at the trailing edge) of approximately $H = 2$ *.

However, the computation (see *table A22*) gave $H = 1{,}475$ instead of $H = 2$. As already pointed out in the 2nd Quarterly Report (§ 1.2.), this seems to be a very complex influence of three-dimensionality on the form of the turbulent boundary layer; the two-dimensional formulae are unable to account for.

A careful and detailed experimental and theoretical investigation should be undertaken (and is planned by the BTZ in the near future) to clarify this point and to build up a three-dimensional formula for the development of H.

3.9.2.6. Meanwhile, the following considerations may be of help: The calculation of the "longitudinal" boundary layer inside the streamstrips and of its form parameter H should be based on the corresponding component of the skin friction, which latter is acting in direction of the wall streamlines and *not* in that of the outer flow.

On the other hand, the value of $\frac{\tau_p}{\rho U_e^2}$ calculated by Squire and Young's formula (§ 1.4.1.2.) for *two*-dimensional flow, is supposed to be an expression of the total skin friction in direction of the wallnear flow. For the calculation of H in the longitudinal flow, only a reduced value $c_r \frac{\tau_p}{\rho U_e^2}$ should therefore be introduced into Von Doenhoff and Tetervin's formula.

At least in the quasi two-dimensional flow in the streamstrip along the symmetry line of the ring airfoil's upper side, we should however expect a reduction factor $c_r = 1$, which is, by virtue of what has been said in § 3.9.2.5., obviously *not* the case.

3.9.2.7. The explanation for this seeming contradiction may be found in the following reflections:

The crossflow, which disappears everywhere for zero incidence, reaches on the flanks of the airfoil considerable strength at the approach of $i_{crit.}$. This crossflow, of various strength through the boundary layer, changes not only the velocity profiles and, consequently, the local form parameter of the turbulent boundary layer, but also the structure of the turbulence inside the layer. Such a change of structure affects not only the local features of the flow, but also, by turbulent interaction, the features (intensity and distribution of the turbulent eddies) in other regions of the flow and — in particular — even in the quasi two-dimensional streamstrip in the symmetry plane ($\varphi = 180°$).

(*) Indeed, the trailing-edge separation seems to be impending, cf. *fig. 1.5.* Taking account of the fact that on the model the last 16 mm of the profile had been cut away for the sake of easier fabrication, we can consider $H = 2$ for $x = 400$ as reasonable.

3.9.2.8. No means of detailed calculation of such an influence of the crossflow on the structure of turbulence — and therefore on the form parameter — being known at present, it has been decided to try a global estimation (justified by the above mentioned interaction which tends to homogenize these effects of three-dimensionality) of the crossflow action by the adoption of a unique value of the reduction factor c_r over the whole upperside of the surface.

In this form, the factor depends, naturally, on λ and i, but not on s and φ; we have $c_r = c_r(\lambda, i)$ *.

c_r should then be determined in such a manner as to get $H \sim 2$ near the trailing edge in the symmetry plane, at $i \sim i_{crit}$.

This has been undertaken in the three experimentally checked cases ($\lambda = 0{,}2$; 0,5 and 1). The result is represented by the curves of *fig. 3.24* and *3.25*.

For $i = 0°$, we have-for all λ's : $c_r = 1$ and thus $c_r\,\alpha = 0{,}0288$ (two-dimensional value in Squire and Young's formula).

3.9.2.9. With the $c_r\alpha$-values thus determined, H has been recalculated, for $i = 15°$ and $\lambda = 1$, in all stream-strips. The corresponding iso-H lines are equally represented in *Graph I*.

3.9.2.10. The formula for turbulent wall streamlines as given by § 1.5.5.,

$$\operatorname{cotg} \theta_p = 0{,}7 \cdot \frac{H - 2}{H - 1{,}286} \cdot \frac{\dfrac{\partial K_p}{\partial s} - c_1}{\dfrac{\partial K_p}{\partial z} - c_2}$$

with $c_2 = 0$ by reason of the obstacle's symmetry, then contains only one unknown quantity : c_1.

This quantity can, in our case, be determined by the following argument (see *Graph I*) :

Save for $\dfrac{\partial K_p}{\partial s} > 0{,}01$, i.e. for values very close to the leading-edge separation and therefore well upstream from any possible reattachment, all $\dfrac{\partial K_p}{\partial s}$ values occur twice and therefore lead to two singular wall streamlines on the turbulent part of the wing's surface.

If c_1 be, therefore, greater than 0,01, no reasonable reattachment point (i.e. $\theta_p = \dfrac{\pi}{2}$. $\operatorname{cotg} \theta_p = 0$, $\dfrac{\partial K_p}{\partial s} - c_1 = 0$, cf. § 2.7.) can be found.

If, on the other hand, $c_1 < 0{,}01$, we shall find two distinct reattachment points or — in the case of $c_1 < 0{,}0075$ — no reattachment point at all. For $c_1 = 0{,}0075$, only one reattachment point would occur, but two different lines with $\theta_p = \dfrac{\pi}{2}$ would have their origin in this point. None of these alternatives seems reasonable.

However, for one particular value of c_1 ($= 0{,}0035$), the second (rearward) branch of $\dfrac{\partial K_p}{\partial s} = c_1$ coincides practically over the whole turbulent region with a branch of $\dfrac{\partial K_p}{\partial z} = 0$ and is therefore cancelled out:

$\left(\dfrac{\partial K_p}{\partial s} - 0{,}0035\right) \Big/ \dfrac{\partial K_p}{\partial z}$ is undetermined and thus $\operatorname{cotg} \theta_p$ not necessarily zero.

For this value of c_1 alone, one and only one reattachment line of reasonable position is possible. For this reason we put $c_1 = 0{,}0035$.

3.9.2.11. It is now possible to calculate, step-by-step, the turbulent wall streamlines on the whole upper surface. The result can be seen in *Graph I:*

We find a non-separated turbulent boundary layer everywhere downstream of the first branch of $\dfrac{\partial K_p}{\partial s} = c_1$. The turbulent wall streamlines in this region can be followed back (upstream) towards the critical branch of $\dfrac{\partial K_p}{\partial s} = c_1$; at its approach, they form a (rearward) envelope; moreover, $\operatorname{cotg} \theta_p$ changes its sign, i.e. the flow changes its direction at the passage of this envelope.

The result is a well-defined reattachment line, limiting a separated-flow area (bubble) against the ordinary (non separated) boundary layer. The configuration thus obtained is qualitatively very similar to the experimental pattern of *fig. 1.5*; moreover, the depth of the bubble is smaller, but still comparable in size to that of the observed one.

3.9.3. The case $i = 18°$ (critical incidence as observed at St-Louis and — cf. *fig. C6* for $i = 21°$ — at Poitiers) admits a similar treatment, again with $c_1 = 0{,}0035$. The second branch of $\dfrac{\partial K_p}{\partial s} = c_1$ coincides here not only with $\dfrac{\partial K_p}{\partial z} = 0$, but — moreover — with $H = 2$.

The corresponding flow pattern is given by *Graph II* and shows a complete reverse flow over the whole central part of the wing's upper surface; instead of a reattachment line at the forward branch of $\dfrac{\partial K_p}{\partial s} = c_1$, we then find the flow pattern of a separation line with (laminar?) boundary-layer flow upstream that line. This has been discussed, in detail, in the 1st Scientific Report.

Even the narrowing of the corridor near the contact of $H = 2$ and what was once the leading-edge bubble (cf. *fig. C6* and *C12*) is correctly represented.

3.9.4. These results seem to confirm the correctness of the foregoing theoretical and numerical considerations, at least in the qualitative agreement between observations and calculations. We are still very far from a reasonable quantitative agreement; moreover, the H distribution could only be obtained by an empirical (and doubtful) determination of c_r. Much work remains therefore to be done.

3.10. The other two cases ($\lambda = 0{,}5$ and $\lambda = 0{,}2$) present still more difficulties:

3.10.1. Indeed, the extreme smallness of the chord compatible with the diameter of the test section at Poitiers, made a correct determination of the trailing-edge separation and therefore of the critical incidence very difficult.

3.10.2. Unfortunately, the complementary phenomenon (large diameter and therefore an abnormal extension of the perimeter of the leading edge) makes a reliable determination of $\dfrac{\partial K_p}{\partial z}$ difficult, if not impossible.

3.10.2.1. As shown by *fig. 3.26* and *3.27*, no line $\dfrac{\partial K_p}{\partial z} = 0$ could be analytically found in these cases (represented is $\lambda = 0{,}2$). The above determination of c_1 therefore does not work in these cases. Experimental checks in order to control the computation of $\dfrac{\partial K_p}{\partial z}$ over the surface of the airfoil are under way at Poitiers, but are not yet concluded.

(*) A more careful and not only global definition of c_r is in hand and will be discussed in a further report. In this case, c_r will depend, equally, on s and φ.

3.10.2.2. There is probably still another explanation of this failure, explanation recently communicated to the author in conversation by Prof. A. YOUNG (Queens, London):

3.10.2.2.1. In two-dimensional flow, a recent work of McGREGOR discussed the difference between "short" and "long" bubbles. The first are characterized by pressure distributions with a high negative peak, steep pressure rise after the minimum and speedy reattachment; they have an almost negligible influence on the theoretical pressure distribution over the profile.

The second are characterized by a pressure distribution with flat minimum, slow pressure rise and retarded reattachment; they have a very great influence on the theoretical pressure distribution over the profile, which is completely changed.

3.10.2.2.2. OWEN recently gave a criterion for long bubbles: they are observed when $\Re_{\delta_1} = \frac{U_e \cdot \delta_1}{\nu} < 450$ at the separation. Now, δ_1 will be — at the same relative position — the smaller in value, the smaller the chord length of the profile is; for $\lambda = 0{,}5$ and $0{,}2$, $\Re_{\delta_1}$ will probably be below this critical value.

3.10.2.2.3. From a physical point of view, the criterion is an expression of the fact that the relative importance in thickness, and therefore the thickness distribution over the wing profile, is different for $\lambda = 1$ and $\lambda = 0{,}5$ and $\lambda = 0{,}2$, and will be more and more difficult to reconcile with WEISSINGER's method, as $\lambda \longrightarrow 0$.

In all these cases, further tests with careful pressure measurements and experimentally obtained values of $\frac{\partial K_p}{\partial z}$ and $\frac{\partial K_p}{\partial s}$ will be necessary. It appears not impossible that with a measured pressure distribution (current practice in boundary-layer work) the method of § 3.9. will once more be applicable.

3.10.3. Nevertheless, it has been possible, from the material so far collected (see *fig. A1 — A8* and *B1 — B12*), to determine even in these two cases the critical incidence with an acceptable precision. This permitted an extrapolation of the i_{crit}-values towards $\lambda = 0$, extrapolation leading to *fig. 3.28*; the result was $i_{crit} = 6^0$ for $\lambda = 0$, in excellent agreement with the already mentioned result of CANNES (cf. § 3.7.1. and [13]).

3.11. On nearly all pictures of the series A, B, C, and particularly well on the *fig. B3*, there can be seen, near the "corners" of the bubble, but not coinciding with them, a pair of dark shadows of roughly triangular shape which are often — as in *A1, B2, C3* and (faintly) even on *fig. 1.5* — prolonged downstream by a line of approximately the direction of the inviscid streamlines.

3.11.1. At closer inspection, on all these pictures — and particularly well on *fig. B6* — it can be established that the reattachment line undergoes, at the passage of this dark shadow, an abrupt change of slope (cf. *fig. 3.29*) :

Indeed, θ_p becomes, at the approach of the corners, suddenly closer to $\frac{\pi}{2}$ than in the inner part (left-hand side in *fig. 3.29*) of the reattachment line.

3.11.2. In *fig. B9*, a scale has been represented on the photo. It allows the estimation :

$$\Re_s = \frac{U_e \cdot s}{\nu} \sim \frac{37 \cdot 0.03}{14} \cdot 10^6 \sim 8 \cdot 10^4$$

This small Reynolds number suggests the explanation that the part of the reattachment line near the corner, with changed slope, corresponds to *laminar* reattachment.

3.11.3. The dark shadow is then an accumulation of the fluid inside the bubble, carried along the separation line towards the corners and unable to enter the corners with their reduced section.

Thus, a drop is forming (which could be directly observed at ST-LOUIS) that breaks through the surface of the (flat) bubble. Then, its upper part is carried away by the outer flow and rains progressively down, thus explaining the straight lines, prolongation of the shadows in downstream direction.

3.11.4. The described computation method (see § 3.9.) is not sensitive enough to take account of the (not very important) laminar part of the reattachment line. Nevertheless, the evidence for laminar reattachment is of interest.

3.12.1. Recently, T.W.F. MOORE reconsidered, in two publications ([14], [15]), the problem of leading-edge bubbles in two-dimensional flow.

3.12.1.1. He confirmed OWEN's criterion, as mentioned in § 3.10.2.2., and associated long-type bubbles ($\Re_{\delta_1} \leq 450$) with a "delayed transition" and, therefore, with laminar reattachment; the same observation has equally been made at the ONERA (Paris) by H. WERLÉ.

3.12.1.2. Short-type bubbles ($R_{\delta_1} > 450$) are, in the same order of ideas, followed by turbulent reattachment, transition taking place already in the shear layer above the bubble.

3.12.2. In his work, MOORE gives an equivalent criterion to that of OWEN, but which is much more "handy" :

3.12.2.1. He introduces a "pressure-recovery coefficient" $\sigma = \frac{K_{p1} - K_{p2}}{1 - K_{p1}}$, formed with the pressure coefficient measured at separation (p_1) and at transition (p_2), cf. the legend to *fig. 3.19*.

3.12.2.2. It is, indeed, easier to measure p_1 and p_2 than to determine δ_1 at the leading-edge separation.

3.12.2.3. If σ increases (which happens for increasing incidence) towards a critical value of about 0,37, the until then short-type bubble becomes all at once of the long type, delaying transition in the shear layer and thus reducing the value of σ which remains always under 0,37.

3.12.3. In three-dimensional flow, as e.g. for the annular wing, p_1 and p_2, and therefore σ are functions not only of incidence, but too of the angular position φ.

3.12.3.1. Thus the character of the bubble may change with φ also, and induce the coexistence of long type and of short types on the same airfoil and even in the same bubble.

3.12.3.2. Reattachment may, therefore, be partly turbulent and partly laminar, which agrees with §§ 3.11.2 and 3.11.3.

3.12.4. Now, the long-type bubbles change completely the pressure distribution on the airfoil; even if only very small portions of the leading-edge bubble are of long type, their (always visible) presence near the bubble's corners have, at least in the wake of this part of the bubble, a strong influence on the pressure distribution in the affected region.

3.12.5. WEISSINGER's method will, therefore, always lead to locally erroneous results when a leading-edge bubble with laminar reattaching corners appears; in particular near the straight dark lines mentioned in § 3.11.3, values of $\partial K_p/\partial s$ and $\partial K_p/\partial z$ will be wrong when calculated with WEISSINGER's method.

3.12.6. The necessity of further carefully executed and systematic measuring tests, expressed in § 3.10.2.2.3.; is thus strongly underlined.

4. Conclusion

4.0. A theoretical method of predicting the development of viscous flow over ring airfoils has been developed at BTZ, in collaboration with ISL, ONERA, the Laboratoire de Mécanique des Fluides de l'Université de Poitiers and the corresponding Laboratoire of the Laval University at Quebec.

This method, which is based on Weissinger's method of determination of the inviscid flow over ring airfoils and on Eichelbrenner's general conceptions of three-dimensional boundary layers in laminar and turbulent flow, permits in certain cases of mean aspect ratio (about $\lambda \sim 1$) even numerical computations of the flow pattern at various incidences and a correct estimation of the critical incidence for three-dimensional stall (contact between leading-edge and trailing-edge separation).

Experimental tests, carried out principally at Poitiers, showed the correctness of the theory's predictions and permitted a detailed control of the essential hypotheses. They permitted, moreover, to pass — for the critical incidence — to the limit $\lambda = 0$ (plane wing) and to state full agreement of this limit with (unpublished) experimental data obtained at the ONERA wind-tunnel in Cannes (France).

Much work remains still to be done; nevertheless, a first step in the direction of actual computation of viscous flow over three-dimensional obstacles in the turbulent case has been accomplished.

Theoretically, the treatment of separation phenomena (leading-edge bubble, reattachment and separation) seems to be well under way.

4.1. It seems that in the foregoing analysis, the following points have been confirmed and may be considered, for future investigations, as established.

4.1.1. The existence and regularity of wall streamlines even in the case of turbulent boundary layers and therefore the correctness of Legendre's "regularity hypothesis" at least for predominantly convex obstacles.

4.1.2. The concept of separation (in laminar and turbulent flow) in three dimensions and the definition of the separation line as limiting wall streamline ("forward envelope" of wall streamlines in a not quite correct, but convenient expression).

4.1.3. The treatment of reattachment as inverse problem of separation (as well in laminar as in turbulent flow) and the definition of the reattachment line as singular wall streamline ("rearward envelope" of wall streamlines).

4.1.4. The explanation of the particular form of stall on the upper side of ring airfoils as contact phenomenon (between leading-edge bubble and trailing-edge separation). This has an immediate application to engineering problems in the case of precambered profiles to avoid or to reduce the leading-edge bubble, as set out in [5] and [11] (foregoing investigations of BTZ).

4.2. The greatest difficulty which has been encountered and which still subsists, is the problem of behavior and structure of turbulent boundary layers in three-dimensional flow, and in particular in regions of strong crossflow. Much work remains to be done, and reliable numerical computation of three-dimensional boundary layers will depend on this point.

4.3. Another very important point is the influence, in function of Reynolds number and aspect ratio, of separated regions on the determination of the inviscid flow over an airfoil. In some cases (as in the foregoing analysis the wings of low aspect ratio, $\lambda = 0{,}5$ and $\lambda = 0{,}2$) the effective form of the obstacle may be so seriously changed by these separated regions and especially by leading-edge bubbles of the "long" type, that the only possibility of determining the pressure distribution in a correct manner seems to be, for the moment, its experimental determination. This is, naturally, unsatisfactory, but a common practice even in the case of laminar two-dimensional boundary layers, e.g. in the simple case of a circular cylinder without yaw (Hiemenz).

4.4. Treatment of compressible flow in three dimensions is in principle possible; indeed, cf. [3], the viscous part of the foregoing method permits, theoretically, an immediate generalization on compressible cases. Practically, it seems to be too early to think of still more complicated calculations, as long as the mentioned difficulties remain.

5. Bibliography

[1] E. A. Eichelbrenner and A. Oudart, ONERA, publication 76 (1955).

[2] H. Schlichting, Grenzschichttheorie, 3. Aufl., Karlsruhe (1958).

[3] E. A. Eichelbrenner, PST du Ministère de l'Air, nº 85 (1959).

[4] E. A. Eichelbrenner, ONERA, publication 89 (1957).

[5] BTZ, Report DA-91-508-EUC 393 (August 1959).

[6] K. Maruhn, ZWB, FB 1174/1 (1940).

[7] E. Truckenbrodt, Ing.-Archiv 20, p. 211-228 (1952).

[8] E. A. Eichelbrenner and R. Michel, La Recherche Aéronautique nº 65 (1958).

[9] E. A. Eichelbrenner and Y. M. Grellier, Note Académie des Sciences (1961).

[10] J. Weissinger, Z.f.W. 3/4, p. 141-150 (März/April 1956).

[11] E. A. Eichelbrenner, Jahrbuch der WGL (1959).

[12] E. A. Eichelbrenner, La Recherche Aéronautique (1961).

[13] E. A. Eichelbrenner, Note Académie des Sciences (1960).

[14] T. W. F. Moore, Journal of the Royal Aeron. Society (Dec. 1959).

[15] T. W. F. Moore, Journal of the Royal Aeron. Society (Nov. 1960).

[16] J. P. Johnston, Journal of Basic Engineering (March 1960).

[17] J. P. Johnston, Journal of Basic Engineering (Sept. 1960).

6. List of Symbols

c_1 coefficient in the cotg ϑ_p formula
c_2 coefficient in the cotg ϑ_p formula
c_f local friction coefficient of the flat plate
c_L coefficient in the cotg ϑ_p formula
c_r reduction factor
c_T coefficient in the cotg ϑ_p formula
i^0 angle of incidence
l reference length
n direction normal to the body's surface
p static pressure
q local dynamic pressure $q = \frac{\rho U_e^2}{2}$
q_∞ dynamic pressure $q_\infty = \frac{\rho U_\infty^2}{2}$
r radial distance from wing axis
s direction of streamlines in the inviscid flow
u streamwise velocity component in the boundary layer
v normal velocity component in the boundary layer
v_x axial velocity
v_{x0} axial velocity produced by the thickness-induced vortex distribution
v_{xq} axial velocity induced by source distribution
v_{x1} axial velocity produced by vortex distribution
v_φ circumferential velocity
w transversal velocity component in the boundary layer
x axial coordinate
x_{tr} transition point
z direction of equipotential lines
D diameter of the annular wing
H form parameter of the turbulent boundary layer $H = \frac{\delta_1}{\delta_2}$
K_p pressure coefficient $K_p = \frac{p - p_\infty}{q_\infty}$
L chord length of the airfoil
$\mathfrak{R}_L$ Reynolds number based on the chord of the airfoil $\mathfrak{R}_L = \frac{U_\infty \cdot L}{\nu}$
$\mathfrak{R}\delta$ — — based on the boundary layer thickness $\mathfrak{R}\delta = \frac{U_e \cdot \delta}{\nu}$
$\mathfrak{R}_s$ — — based on the local distance $\mathfrak{R}\delta = \frac{U_e s}{\nu}$
$\mathfrak{R}_{\delta_1}$ — — based on the displacement thickness $\mathfrak{R}_{\delta_1} = \frac{U_e \cdot \delta_1}{\nu}$
U_e velocity at the edge of the boundary layer
U_∞ free stream velocity
$\vec{V}$ flow vector inside the boundary layer
α coefficient in SQUIRE and YOUNG's formula
δ boundary-layer thickness
δ_1 displacement thickness
δ_2 momentum-loss thickness
ϑ angular coordinate
λ aspect ratio of the ring airfoil $\lambda = \frac{L}{D}$
ν kinematic viscosity
ξ dimensionless axial coordinate
ϱ reduced radial distance from axis
ϱ air density
τ_p wall shear stress
φ azimuthal angle
ϑ angle between flow direction at the outer edge of the boundary layer and flow direction inside it
Λ POHLHAUSEN's laminar form parameter

Indices

g denotes quantities for a guided vein
p at the wall

7. List of Tables

Table 3.1. List of incidences in function of λ

3.2.1. $\lambda = 0,2$ $U_\infty \approx 45$ m/s Leading-edge separation for various incidences
3.2.2. $\lambda = 0,2$ $U_\infty \approx 45$ m/s Reattachment lines for various incidences
3.3.1. $\lambda = 0,5$ $U_\infty \approx 37$ m/s Leading-edge separation for various incidences
3.3.2. $\lambda = 0,5$ $U_\infty \approx 37$ m/s Reattachment lines for various incidences
3.4.1. $\lambda = 1$ $U_\infty \approx 27$ m/s Leading-edge separation for various incidences
3.4.2. $\lambda = 1$ $U_\infty \approx 27$ m/s Reattachment lines for various incidences
3.4.3. $\lambda = 1$ $U_\infty \approx 27$ m/s Trailing-edge separation for incidence 22°

---

8. List of Figures

Fig. 0.1 System of curvilinear coordinates (s, z, n)

1.1, 1.2, 1.3 Ellipsoid $i = 10°$ — 1.1 Side-View of the rear part; 1.2 View on the upper side of the rear part; 1.3 3/4 View from behind

1.4 Calculated wall streamlines with different c_T in the cotg θ_p formula

1.5 $\lambda = 1$, $i = 15°$, Flow configuration (St-Louis)

1.6 H computed after Doenhoff and Tetervin in function of s for different incidences, $\lambda = 1$, $\varphi = 180°$

2.1, 2.2, 2.3 Configuration of wall streamlines

3.1 System of coordinates applied in Weissinger's method

3.2 Profile-thickness distribution after Weissinger for NACA 66-006

3.3 $\lambda = 1$ $i = 0°$
3.4 $\lambda = 1$ $i = 9°$
3.5 $\lambda = 1$ $i = 15°$
3.6 $\lambda = 1$ $i = 18°$
3.7 $\lambda = 1$ $i = 21°$
— distribution of pressure coefficient K_p in function of ξ

3.8 $\lambda = 0,2$ $i = 6°$
3.9 $\lambda = 0,5$ $i = 9°$
3.10 $\lambda = 1$ $i = 15°$
— theoretical distribution of $\frac{U_s}{U_\infty}$ in function of s

3.11 Model $\lambda = 0,2$

3.12 Streamlines of potential flow far from the wall

3.13 Theoretical lift in function of $i°$ for different λ

3.14 Model $\lambda = 0,5$

3.15 Model $\lambda = 1,0$

3.16 Variation of $\Delta i°$ with incidence

3.17 Flow configuration at the leading edge

3.18 Wall streamline configuration

3.19 Pressure distribution at $\varphi = 180°$ of a ring airfoil with incidence and its relation to the flow configuration

3.20 Configuration of wall streamlines

3.21 $\lambda = 0,2$, $U_\infty \approx 45$ m/s
a. Reattachment lines at various incidences
b. Depth of the separation bubble measured on $\varphi = 180°$

3.22 $\lambda = 0,5$, $U_\infty \approx 37$ m/s Reattachment lines at various incidences

3.23 $\lambda = 1,0$, $U_\infty \approx 27$ m/s
a. Reattachment lines at various incidences
b. Evolution of leading-edge separation at various incidences
c. Evolution of the leading-edge separation measured on $\varphi = 180°$
d. Depth of the separation bubble measured on $\varphi = 180°$

3.24 Variation of $c_r \alpha$ with λ for different incidences

3.25 Variation of critical $c_r \alpha$ with λ

3.26 $\lambda = 0,2$, $i = 6°$ Lines of iso $\frac{\partial K_p}{\partial s}$ and iso $\frac{\partial K_p}{\partial z}$

3.27 $\lambda = 0,2$, $i = 9°$ Lines of iso $\frac{\partial K_p}{\partial s}$ and iso $\frac{\partial K_p}{\partial z}$

3.28 Variation of critical incidences with λ

3.29 Model of flow configuration at the leading edge (Principle Scheme)

Fig. A1 — A8
B1 — B12
C1 — C12
D1 — D3
} Photos for { $\lambda = 0{,}2$ / $\lambda = 0{,}5$ / $\lambda = 1{,}0$

Graph I $\lambda = 1$ $i = 15°$
Graph II $\lambda = 1$ $i = 18°$
} calculated wall streamlines

---

9. Annex *

Tables A1 — A3 Elementary velocities calculated after WEISSINGER's method
A4 — A15 K_p after WEISSINGER's method for the different $\lambda's$ and incidences
A16 — A21 δ_2 calculated after TRUCKENBRODT's formula for the different $\lambda's$ and incidences
A22 H in function of s for $\lambda = 1$ and different incidences.

(*) These tables are not included in the present report; they are available, upon request, at the ONR or at the BTZ.

TABLE 3.1.

List of incidences in function of λ.

λ	0,2	0,5	1,0
incidences	3°	9°	9°
	6°	12°	15°
			18°
	9°	15°	21°
critical incidences	~ 9°	~ 14°	~ 21°

Test Results for
$\lambda = 0,2$
$U_\infty \approx 45$ms

TABLE 3.2.1.

Leading-edge separation for various incidences

Incidence	3°	6°	9°
ζ*	downstream position of separation line (mm from leading edge)		
— 500	3		
— 450		4	
— 400			11
— 350			14,5
— 300		4,5	18,5
— 250	3,5		
— 200		5,5	20,5
— 150			
— 100			21
— 50			
0	4	8	22
+ 50			
+ 100			21
+ 150			
+ 200		5	21
+ 250	3,5		
+ 300		4	18
+ 350			15
+ 400			11
+ 450		3,5	7
+ 500	3		4

* ζ = the development in mm of the wing from φ = 180°.

Test Results for
$\lambda = 0,2$ $U_\infty \approx 45$ m.s

TABLE 3.2.2.

Reattachment lines for various incidences

Incidence	3°	6° 1st test	6° 2nd test	8°	9° 1st test	9° 2nd test	9,50°
ζ*	downstream position of reattachment li (mm from leading edge)						
— 600				9	10	10	11
— 550			10	13	18	18	15
— 500	9,5	11	12,5	21	23	24	23
— 450	11,5	14		31	32	33	35
— 400		27	30	45		49	
— 350	11,5	30		58	60	71	78
— 300	11,5	40	43	78	87	94	106
— 250	14	45	53	96	108	117	145
— 200	14	59	59	108	129	143	182
— 150	13,5	58	58,5	113	160		
— 100	12	56	58,5	120			
— 50	12	57	58				
0	11	62	58,5	126			
+ 50	13	60	60				
+ 100	15	62	60				
+ 150	14	60	60	120	184		
+ 200	13,5	55	57	116	160	153	180
+ 250	13	50	48	96	125	127	143
+ 300	10,5	42	43	76	89	108	103
+ 350	10	36		57	72	75	78
+ 400	9,5	30	27		42	55	53
+ 450		18	18	32	37	37	35
+ 500		12	12,5		28	26	23
+ 550			11		14	17	16
+ 600						11	11

* ζ = the development in mm of the wing from φ = 180°.

Test Results for
$\lambda = 0{,}5$
$U_\infty \approx 37$ m/s

TABLE 3.3.1.
Leading-edge separation for various incidences

Incidence	6°	9°	12°	13°	13,50°	14°
ζ *	downstream position of separation line (in mm)					
— 300		4,5				
— 250			6	5		
— 200		7	9	9		13
— 150			14	17,5	10	22
— 100			16	20	18	24
— 50					22,5	25
0	6	10	19	21,5	23,5	26
+ 50					22	25,5
+ 100			18	21	16	25
+ 150			17	17	8	19
+ 200		8	12	10		13
+ 250			9	8		6
+ 300		5	7	5		

TABLE 3.3.2.
Reattachment lines for various incidences.

Incidence	6°	9°	12°	13°	13,50°	14°
ζ *	downstream position of reattachment line (mm)					
— 350		11	15	11	11	11,5
— 300		13	25	21	27	26
— 250	12	26	48	58	64	65
— 200	16	39	90	105	110	0
— 150	27	69	132	160	165	172 (± 5)
— 100	36	89	155	206	225	220 (± 5)
— 50	41	98	185 (± 5)	240 (± 5)	270 (± 5)	275 (± 10)
0	40	102	200 (± 10)	250 (± 10)	290 (± 10)	
+ 50	36	97	185 (± 5)	235 (± 5)	265 (± 5)	275 (± 10)
+ 100	32	88	161	196	207	234 (± 5)
+ 150	27	70	122	150	165	188 (± 5)
+ 200	22	53	83	110	115	124
+ 250	14	37	40	66	72	74
+ 300		16	18	28	32	36
+ 350		12	12	12,5	10	12

* ζ = the development in mm of the wing from $\varphi = 180°$.

Test Results for
$\lambda = 1$
$U_\infty \approx 27$ m/s.

TABLE 3.4.1.
Leading-edge separation for various incidences.

Incidence	9°	15°	18°	21°	22°
ζ *	downstream position of separation line (mm from leading edge)				
— 200		2	5	6	11,5
— 150	5	6,5	14	17	24
— 100	5,5	18	27	30	37
— 50	7	25	33,5	38	40
0	8,5	26	35	40	42
+ 50	8	25	33	38,5	41
+ 100	6	19	27	33	39
+ 150	5	7	14	17	25
+ 200		2	5,5	6,5	12

TABLE 3.4.2.
Reattachment lines for various incidences.

Incidence	9°	15°	18° 1st test	18° 2nd test	19,50°	21° 1st test	21° 2nd test	22°
ζ *	downstream position of reattachment line (mm from leading edge)							
— 250		5	6		6		15	28
— 200		14	39	37	47	60	62	98
— 150	15	71	99	100	120	135	147	170
— 100	37	128	178	182	202	210	210	256
— 50	54	175	242	232	260	280	283	315
0	65	212	277	278	300	323	330	343
+ 50	58	172	246	250	255	281	286	[illegible]
+ 100	38	122	184	187	185	220	225	245
+ 150	16	65	101	105	96	139	140	172
+ 200		19	39	39	42	65	70	90
+ 250		6	7	6	7		12	

TABLE 3.4.3.
Trailing-edge separation for incidence 22°

ζ *	— 65	— 25	0	+ 25	+ 55
upstream position of separation line (mm from trailing edge)					
	0	36	34	25	0

* = ζ the development in mm of the wing from φ = 180°.

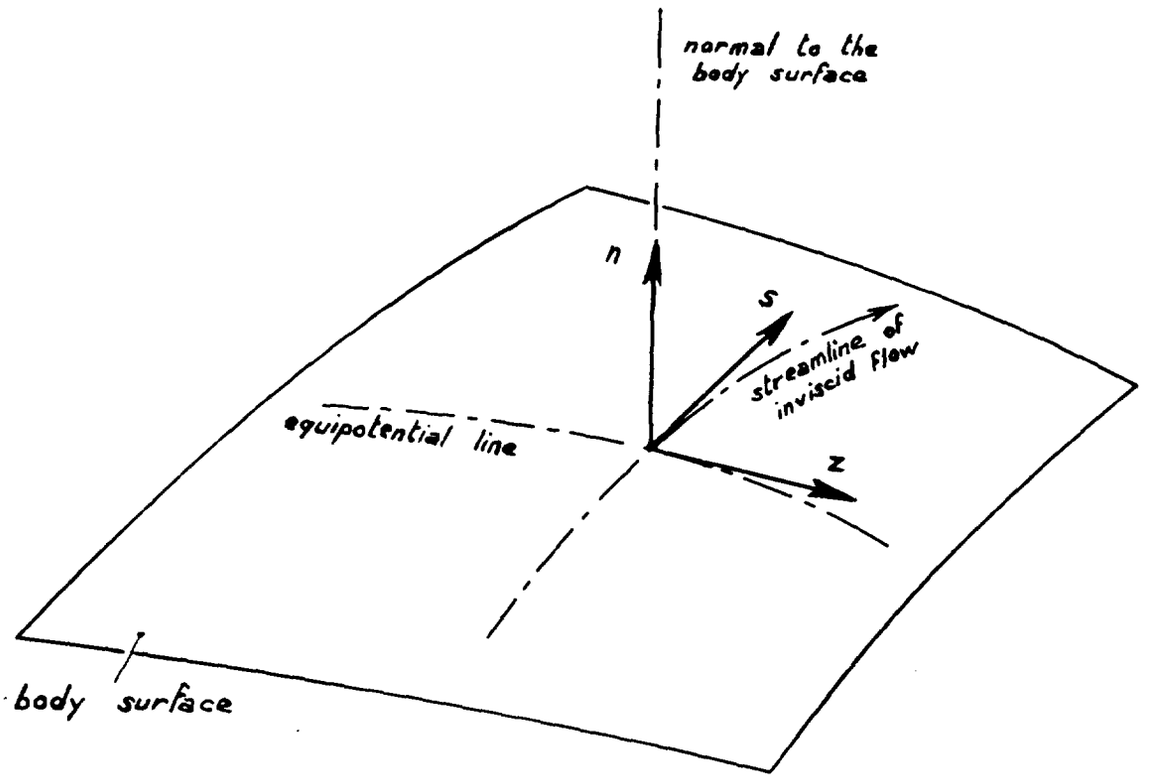

Fig. 0.1. — System of curvilinear coordinates (s, z, n) utilized throughout this report (position of the coordinate trihedral at the wall)

Fig. 1.1 Ellipsoid σ 10% Side-view of the Rear Part.

Fig. 1.2. Ellipsoid σ 10% View of the Upper Side of the Rear Part.

Fig. 1.3. Ellipsoid σ 10% $\frac{3}{4}$-View from Behind.

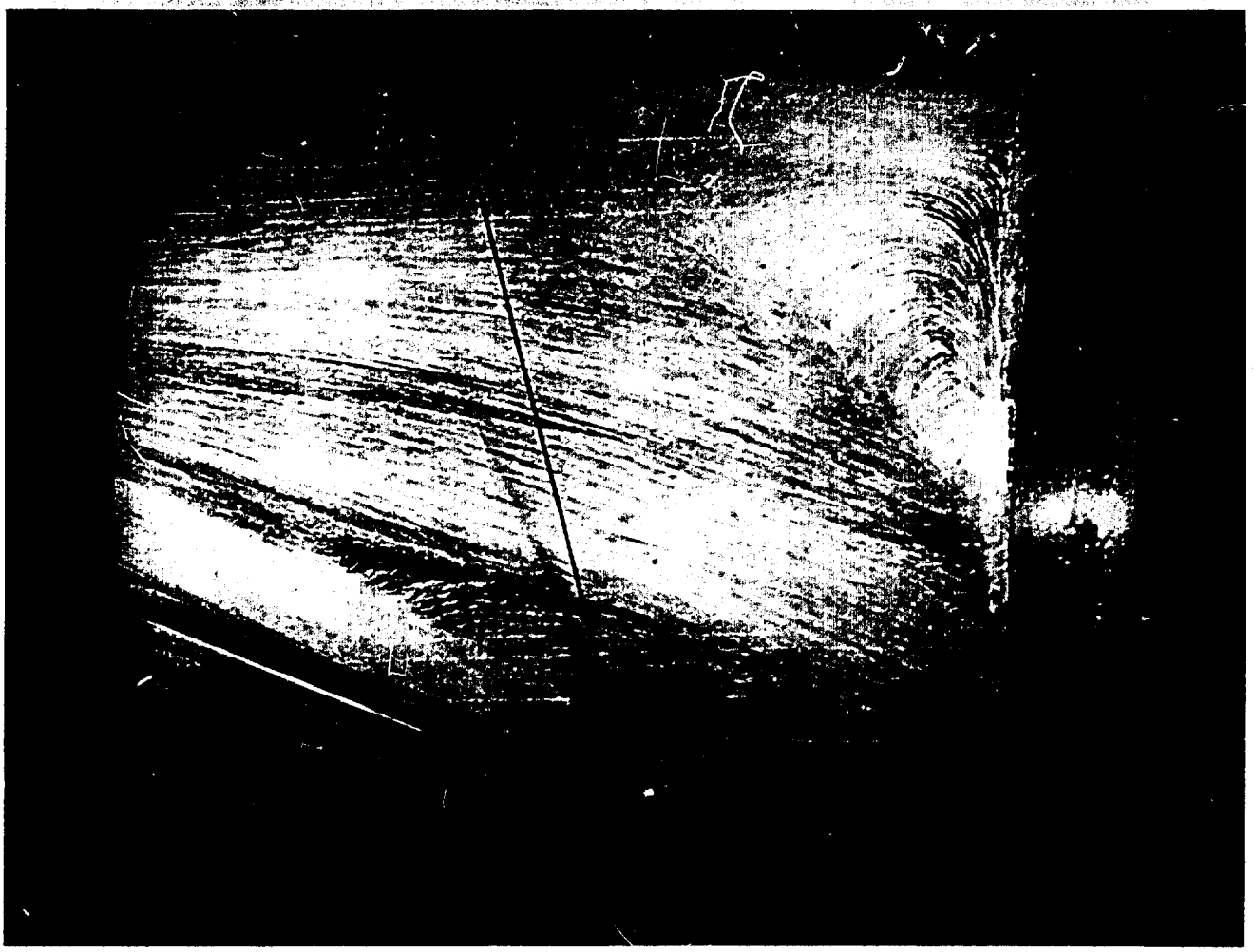

Fig. 1.5. $\lambda = 1$, $i = 15°$, Flow Configuration (ST. LOUIS)

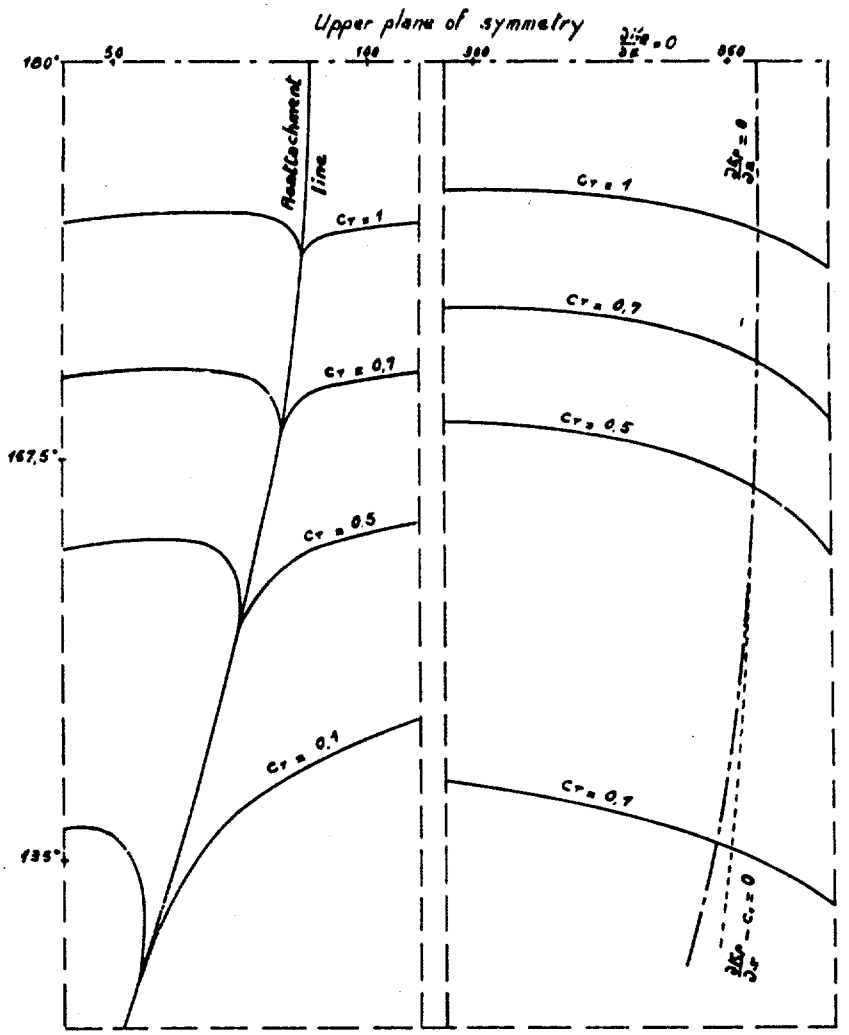

Fig. 1.5.

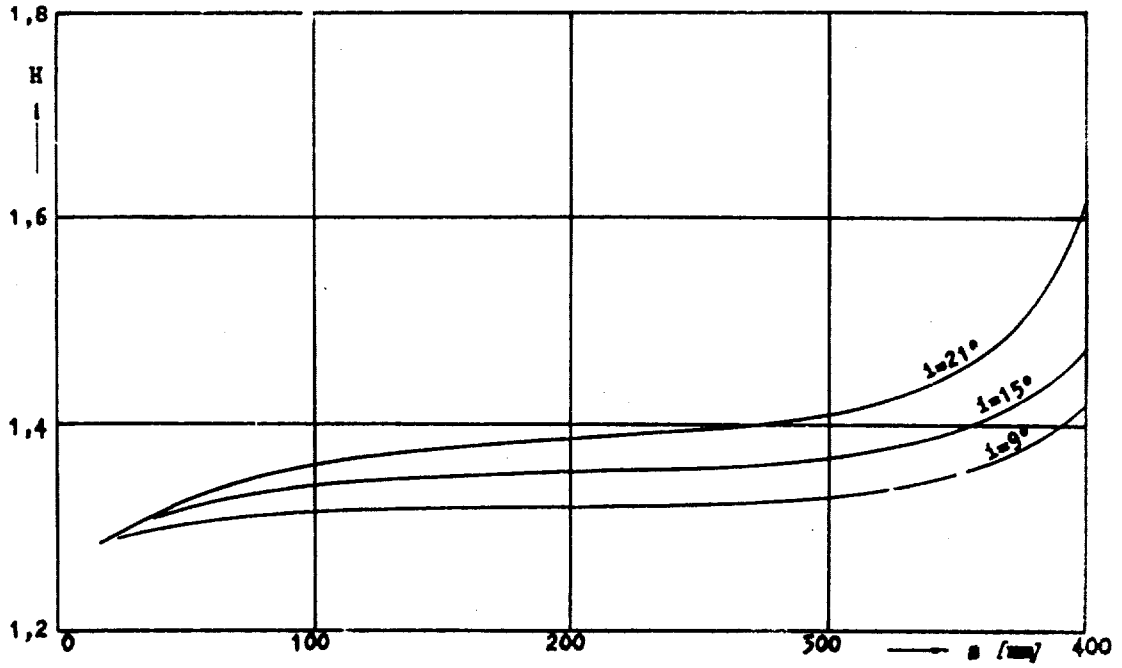

Fig. 1.6. -- Variation of form parameter H in the symmetry plane of ring airfoil $\lambda = 1$ for different incidences (computed after DOENHOFF and TETERVIN)

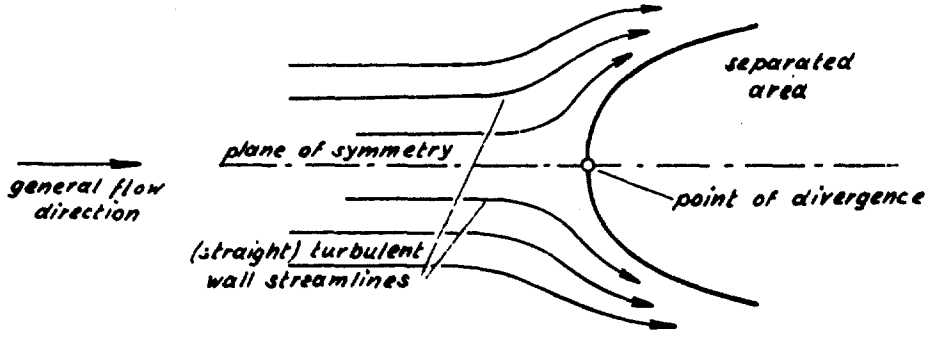

Fig. 2.1

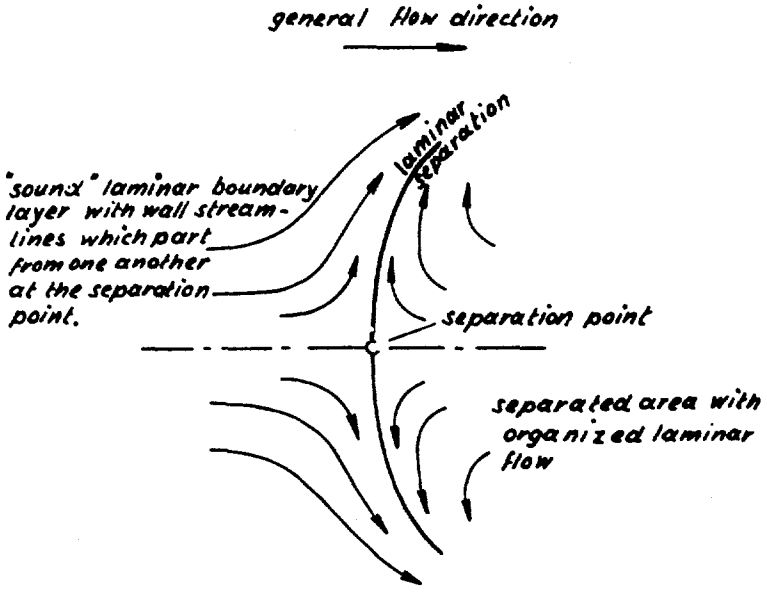

Fig. 2.2

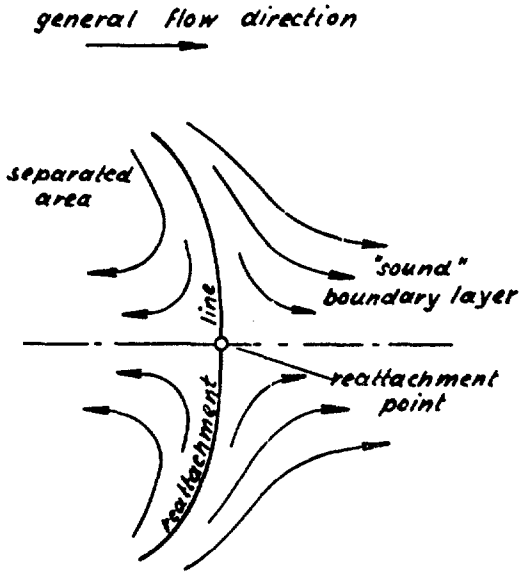

Fig. 2.3

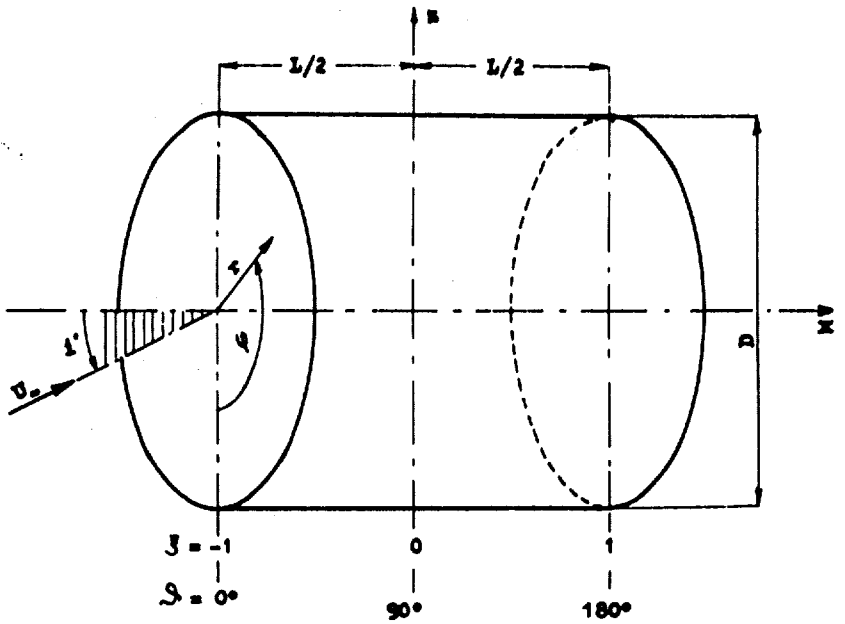

Fig. 3.1. — Coordinates applied in WEISSINGER'S Method.

$$\xi = \frac{2x}{L} = -\cos\vartheta$$

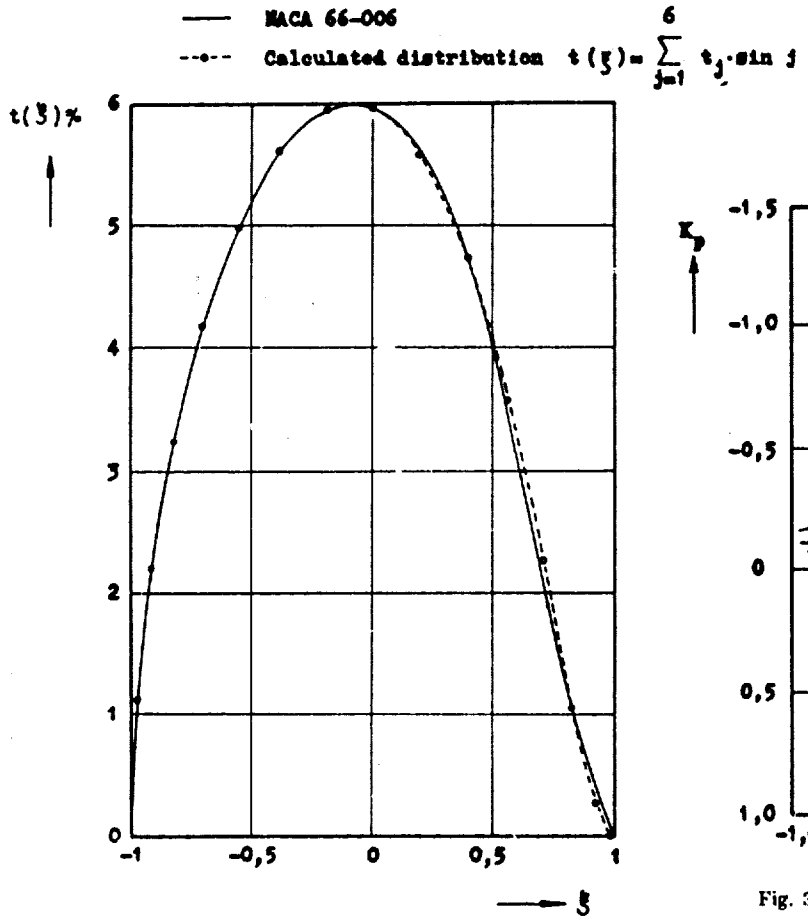

Fig. 3.2. — Profile-thickness distribution.

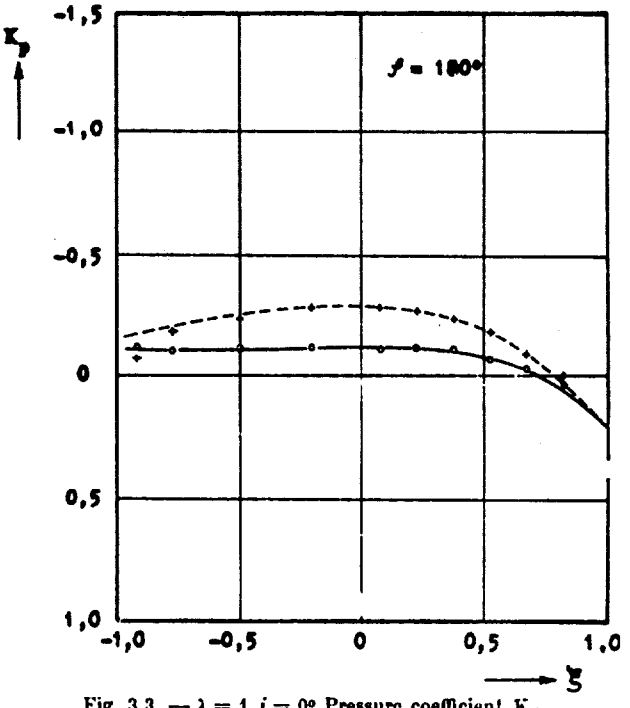

Fig. 3.3. — $\lambda = 1$ $i = 0°$ Pressure coefficient K_p.

Inside ····· calculated.
\+ measured.
Outside —— calculated.
o measured.

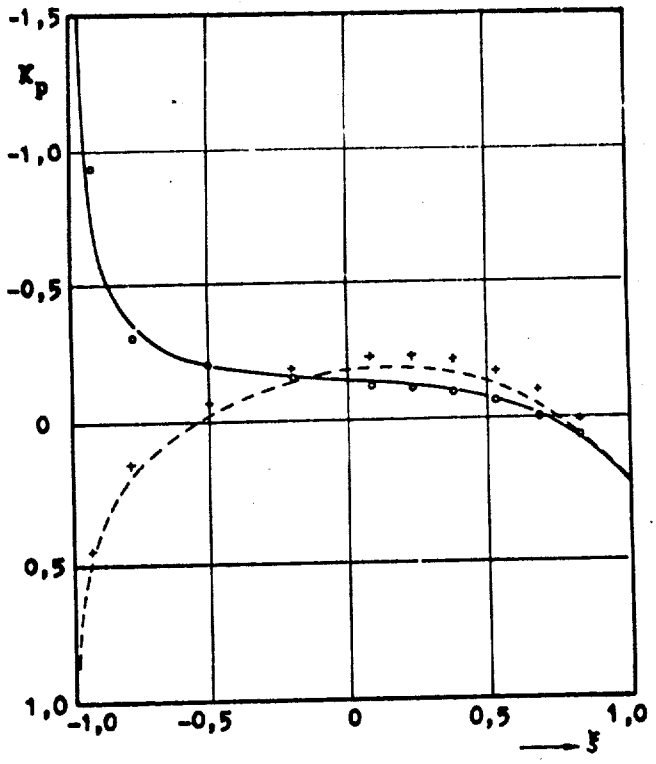

Fig. 3.4.
$i = 18°$

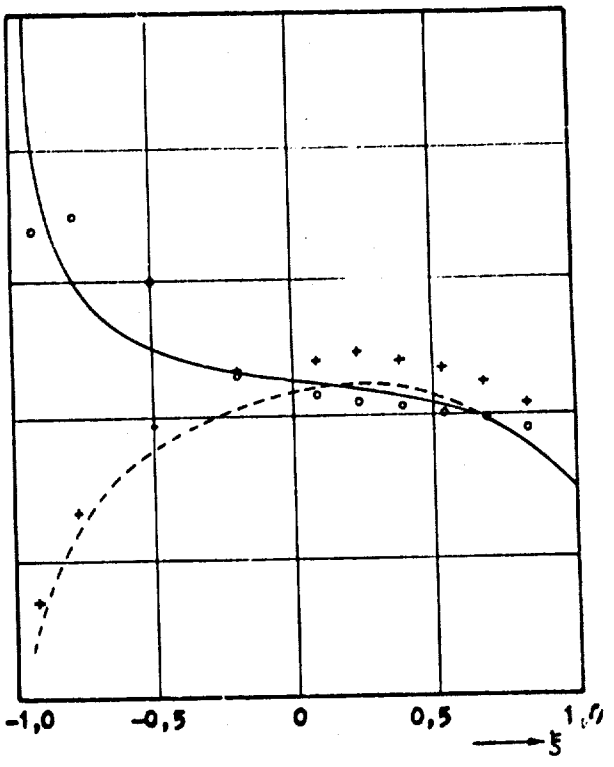

Fig. 3.5.
$i = 15°$

$\lambda = 1$, $\varphi = 180°$

Pressure coefficient K_p

Inside ····· calculated. + measured. Outside —— calculated. o measured.

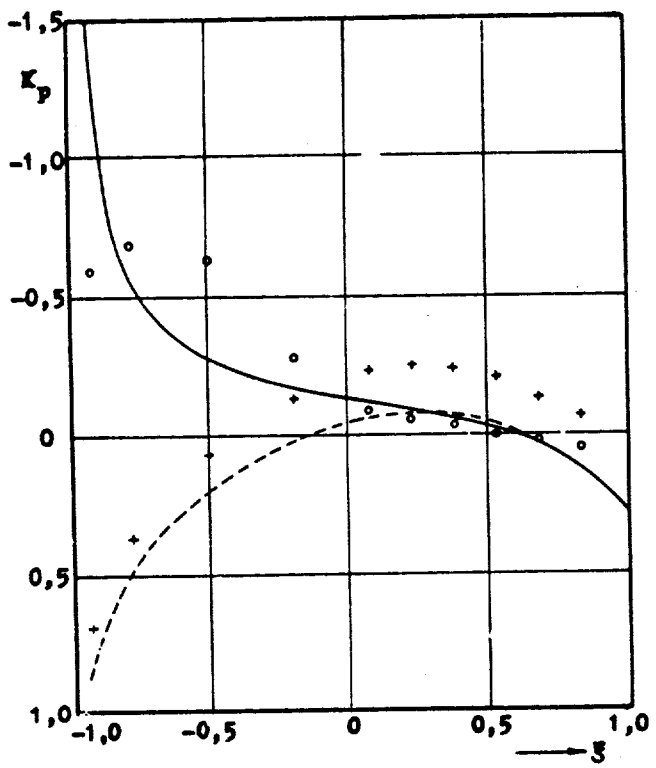

Fig. 3.6.
$i = 18°$

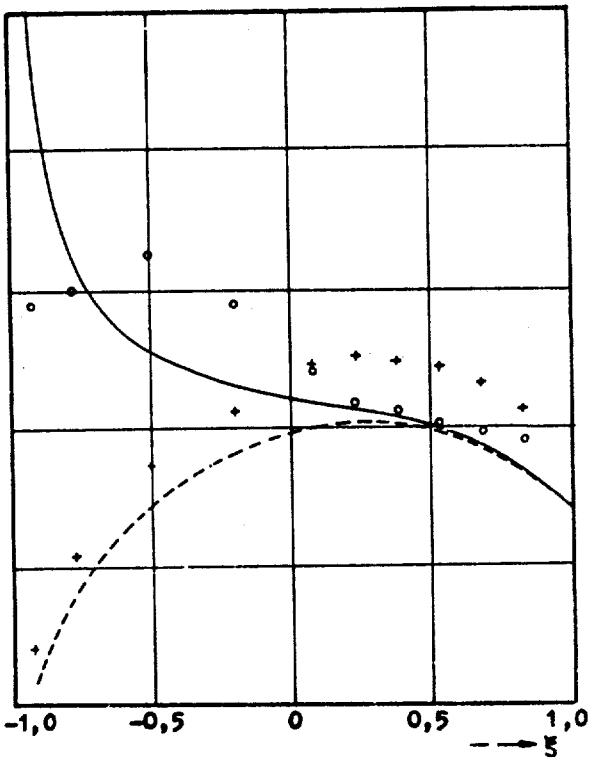

Fig. 3.7.
$i = 21°$

$\lambda = 1$, $\varphi = 180°$

Pressure coefficient K_p

Inside ····· calculated. + measured. Outside —— calculated. o measured.

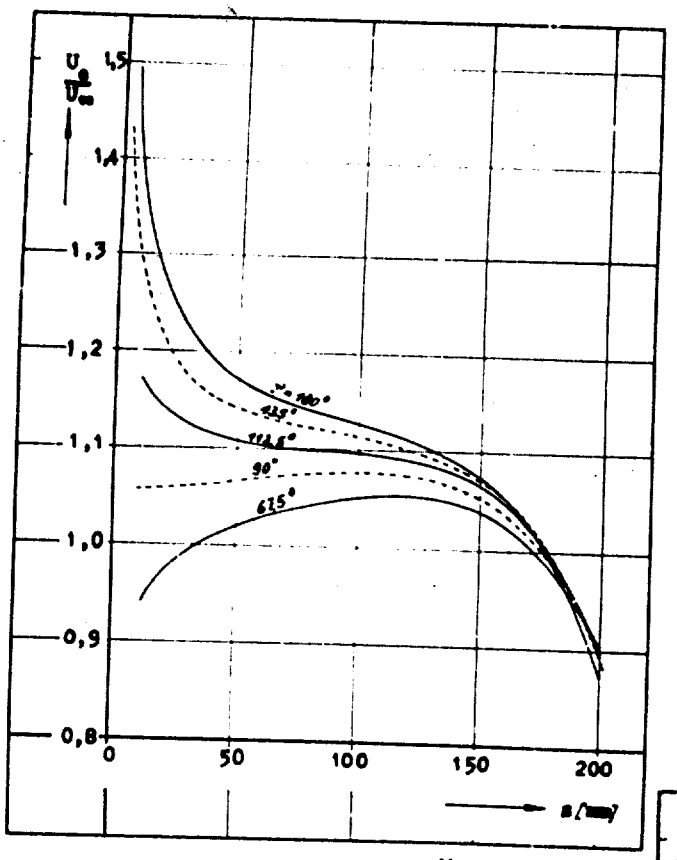

Fig. 3.8. — Theoretical Distribution of $\frac{U_e}{U_\infty}$ in function of s

$\lambda = 0{,}2 \quad i = 6°$

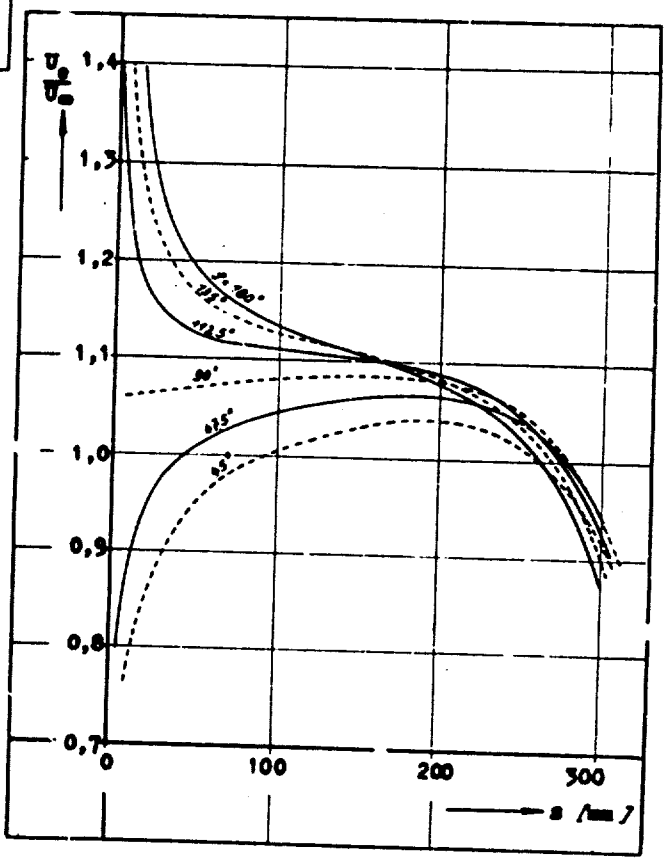

Fig. 3.9. — Theoretical Distribution of $\frac{U_e}{U_\infty}$ in function of s

$\lambda = 0{,}5 \quad i = 9°$

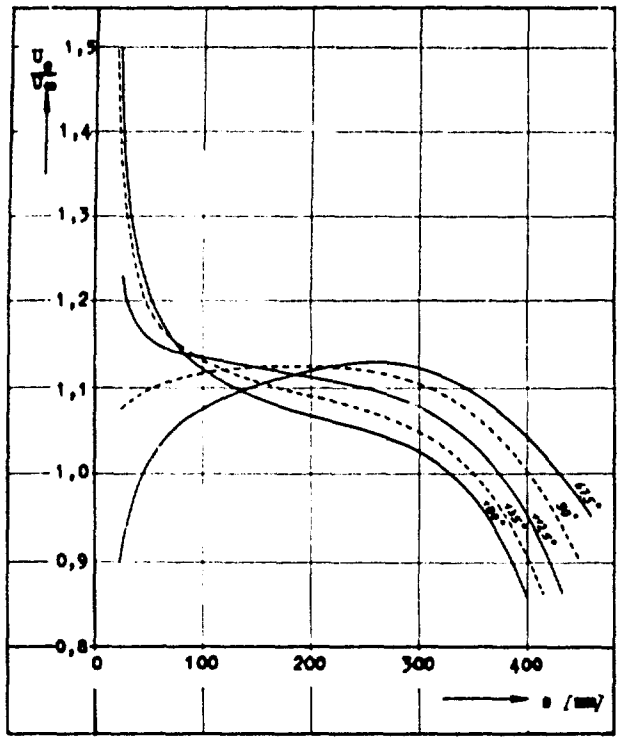

Fig. 3.10.
Theoretical Distribution of $\frac{U_z}{U_\infty}$ in function of s
$\lambda = 1$ $i = 15°$.

PROFILE NACA 66-006

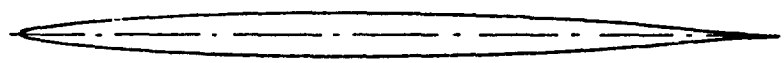

$\lambda = 0{,}20$

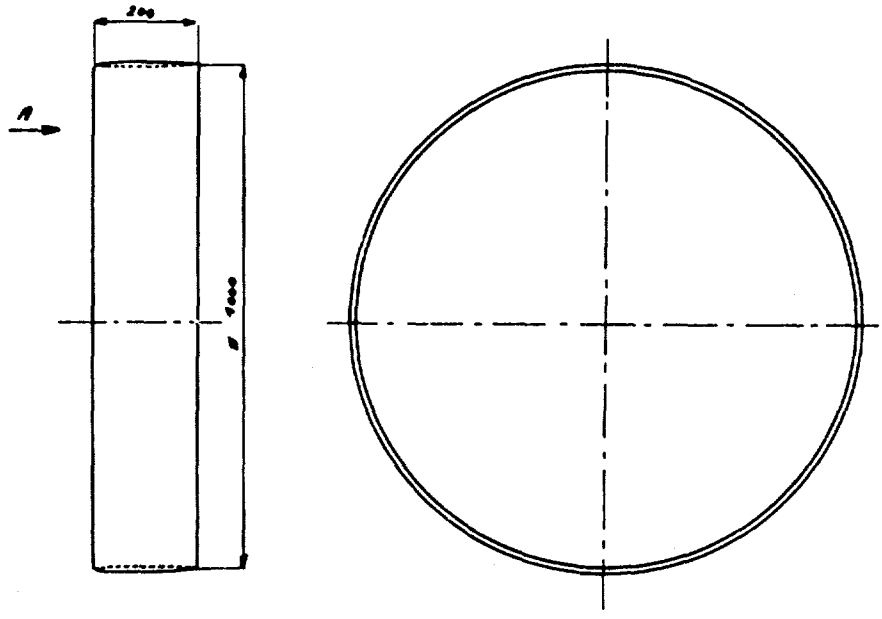

Fig. 3.11.

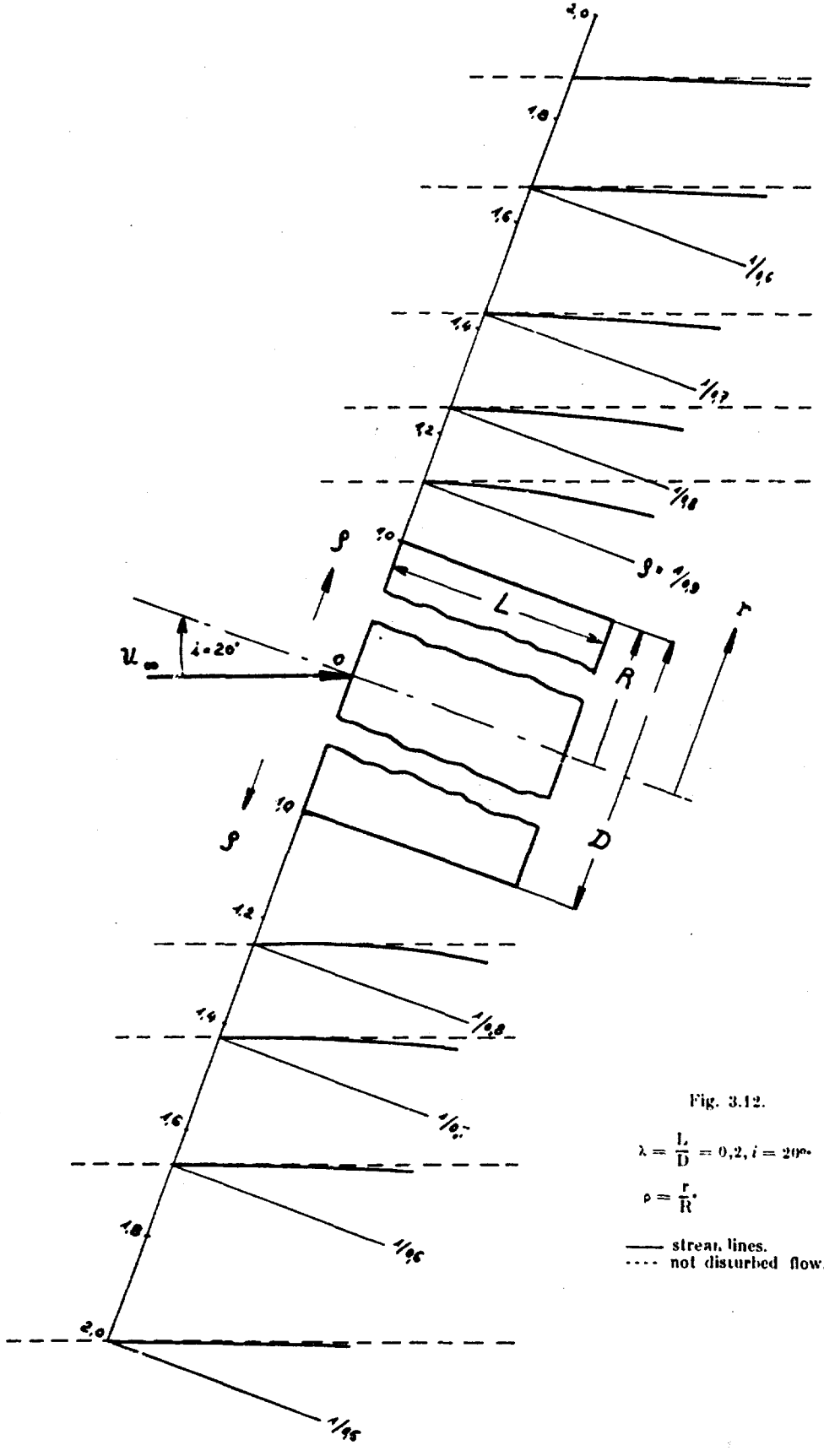

Fig. 3.12.

$\lambda = \frac{L}{D} = 0{,}2,\ i = 20°$

$\rho = \frac{r}{R}$.

—— strean. lines.
···· not disturbed flow.

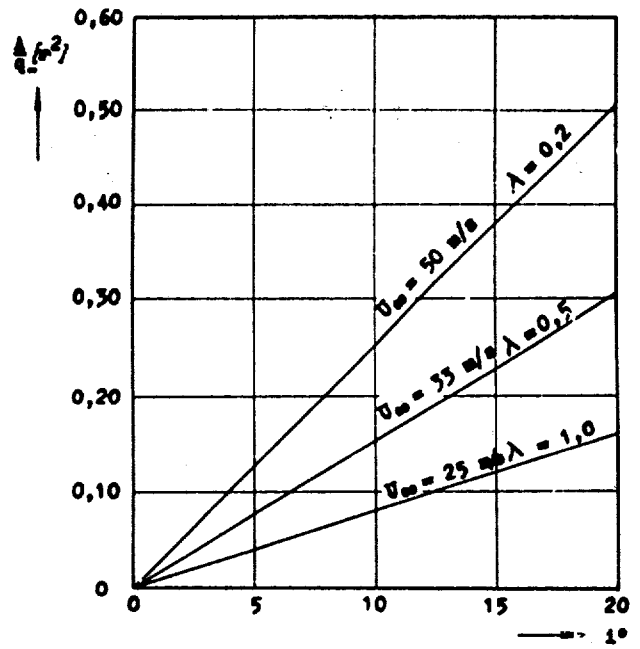

Fig. 3.13. Theoretical Lift.

$A = q_\infty \cdot S \cdot c_l' \cdot i.$

$q_\infty = \rho \frac{U_\infty^2}{2} \qquad S = \frac{\pi D^2}{4}.$

PROFILE NACA 66-006

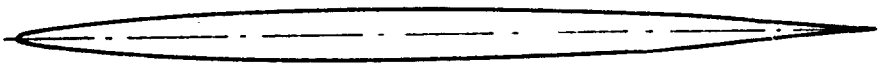

$\lambda = 0{,}5$

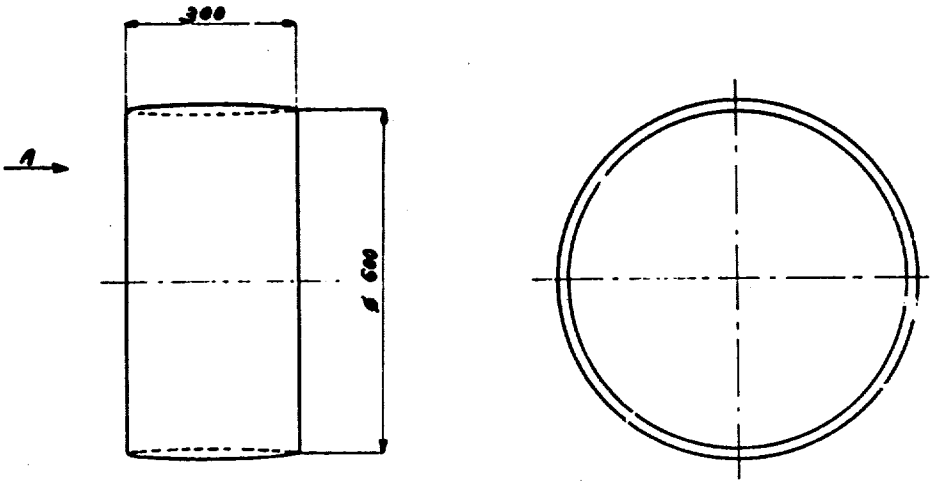

Fig. 3.14.

View from A

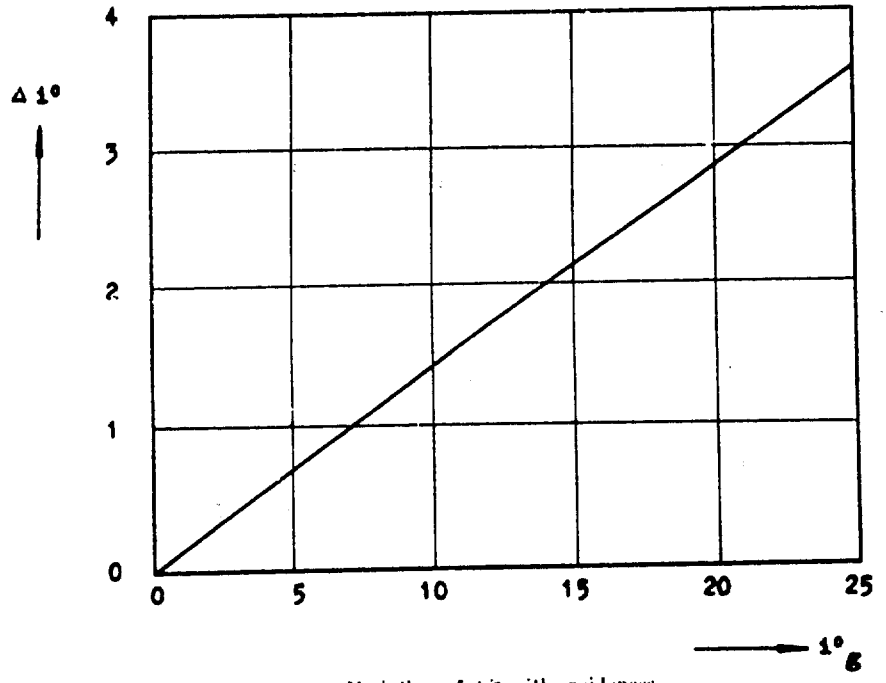

Fig. 3.16. — Variation of $\Delta i°$ with incidences.

PROFILE NACA 66-006

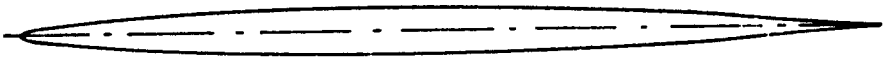

$\lambda = 1$

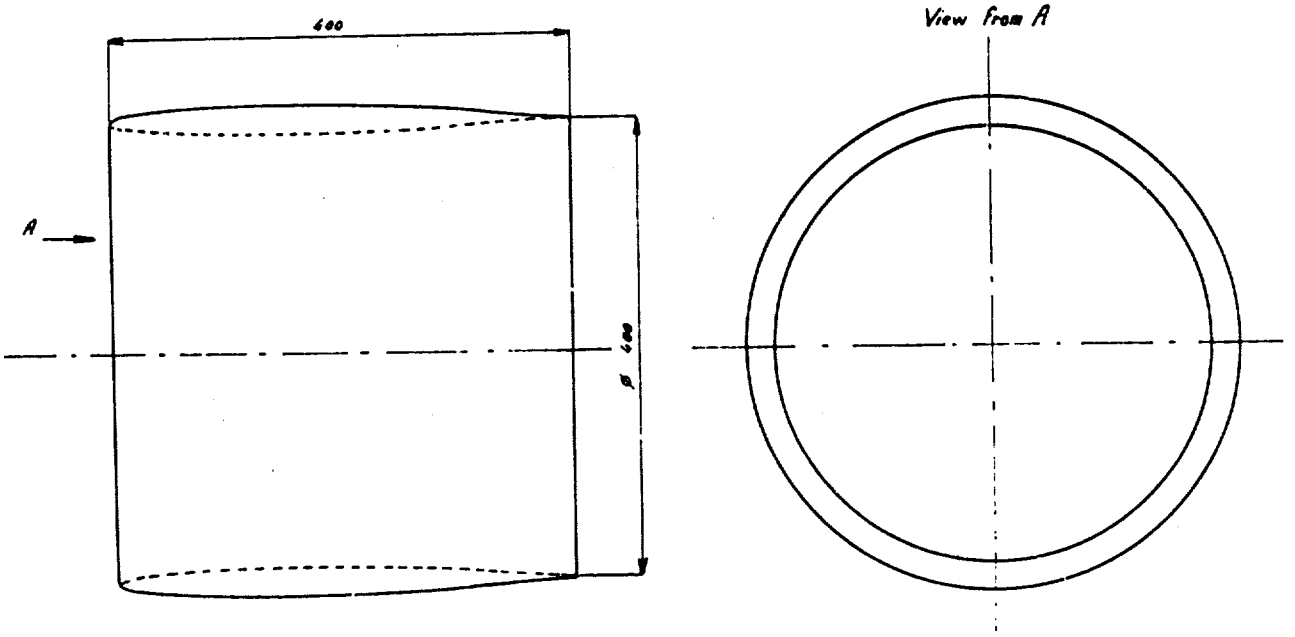

Fig. 3.15.
N.B. All dimensions are given in mm.

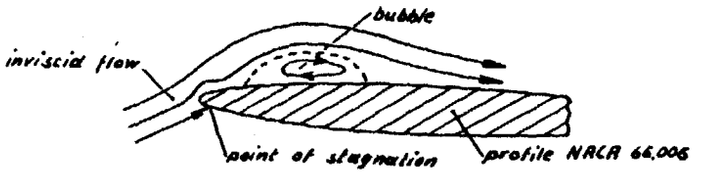

Fig. 3.17.
Flow configuration at the leading edge.

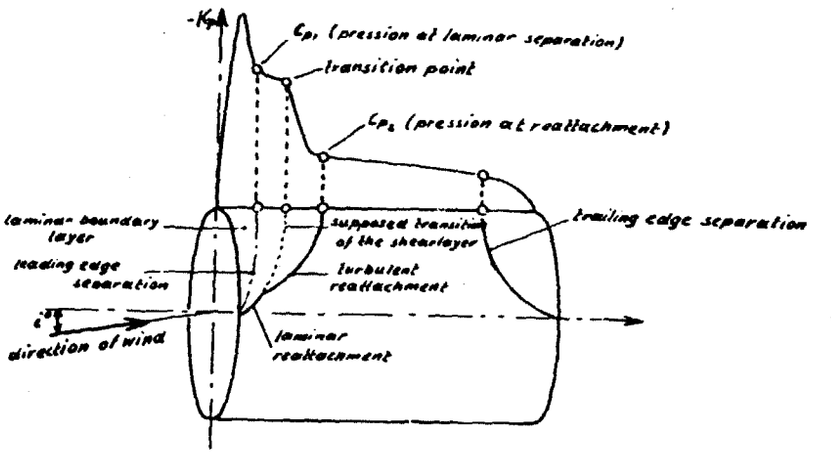

Fig. 3.19.
Pressure distribution at $\varphi = 180°$ of a ring airfoil with incidence and its relation to the flow configuration.

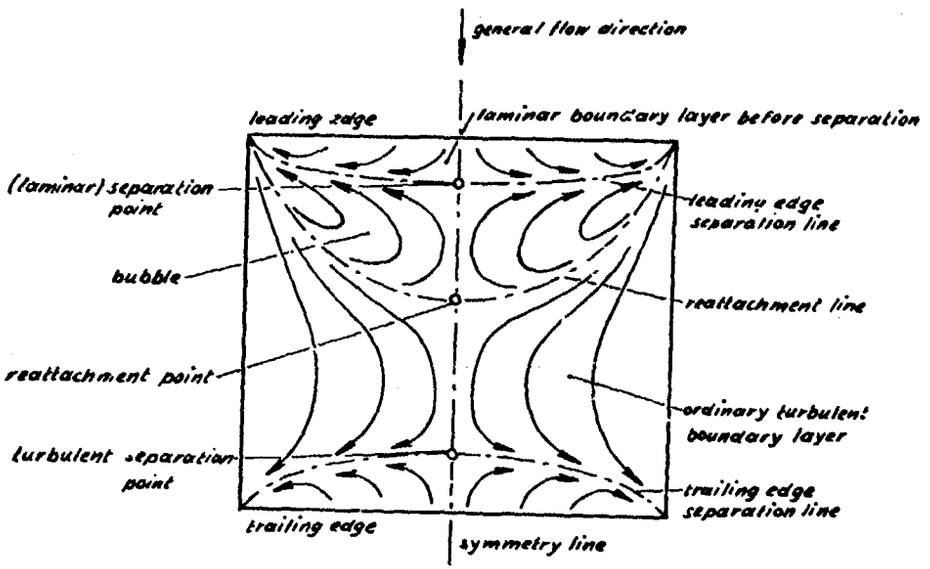

Fig. 3.18.
Configuration of Wall Streamlines.

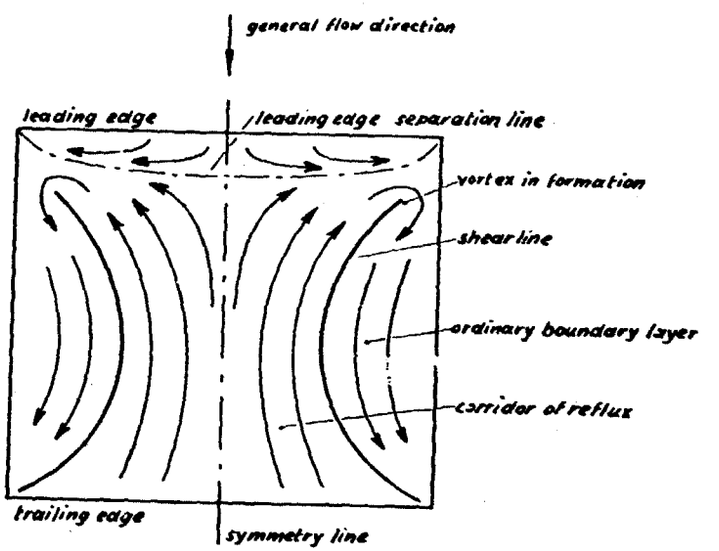

Fig. 3.20.
Configuration of Wall Streamlines.

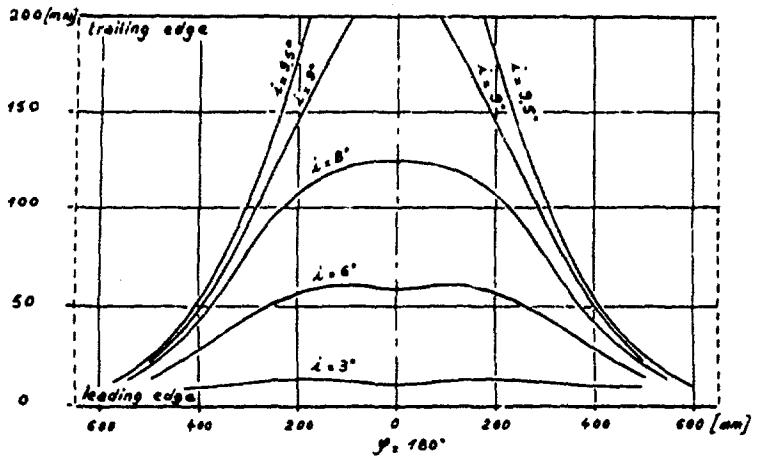

Fig. 3.21.
$\lambda = 0{,}2$
$U_\infty \approx 45$ m/s

a. Reattachment lines at various incidences.

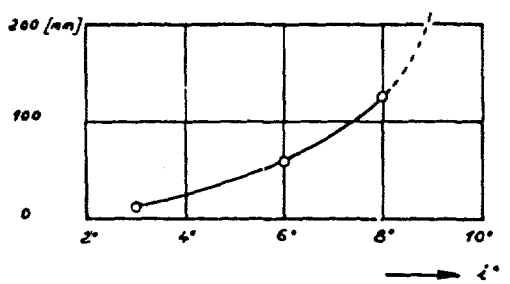

b. Depth of Bubble measured on $\varphi = 180°$ in function of incidences.

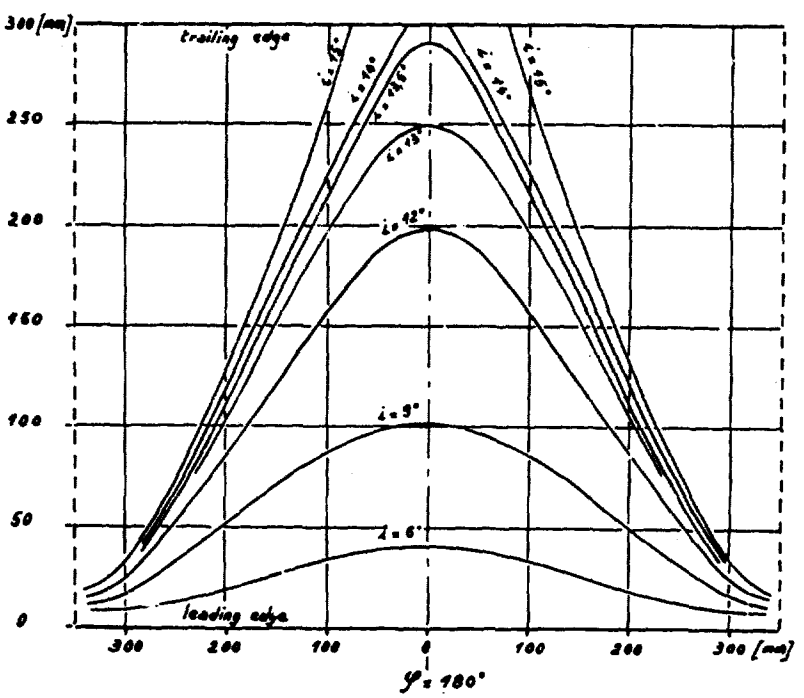

Fig. 3.22.
$\lambda = 0{,}5$
$U_\infty \approx 37$ m/s

Reattachment lines at various incidences.

Fig. 3.23.
$\lambda = 1$
$U_\infty \approx 27$ m/s

a. Reattachment lines at various incidences

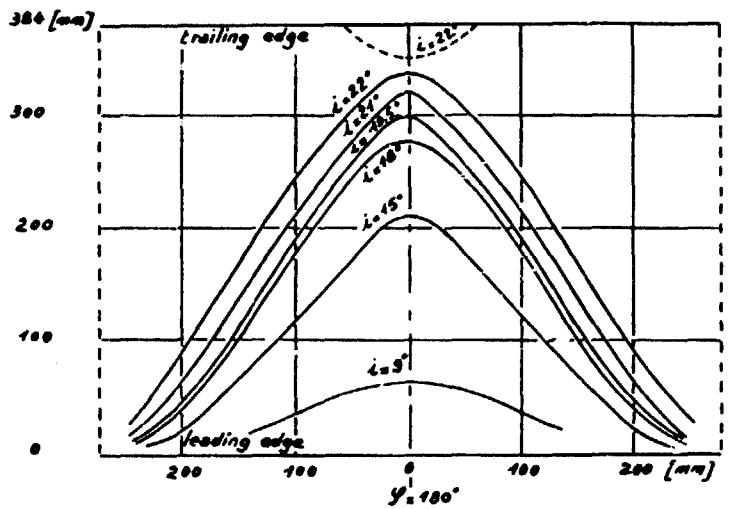

b. Evolution of the leading-edge separation at various incidences

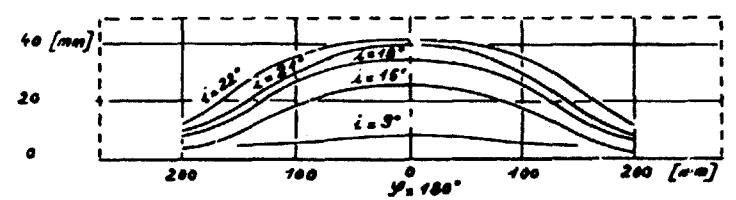

c. Evolution of the leading-edge separation on the symmetry line ($\varphi = 180°$)

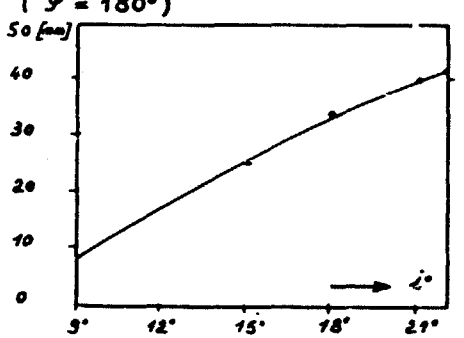

d. Depth of the separation-bubble measured on $\varphi = 180°$

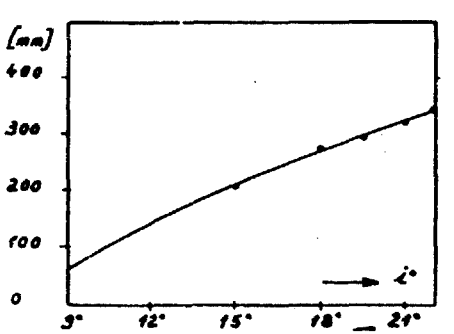

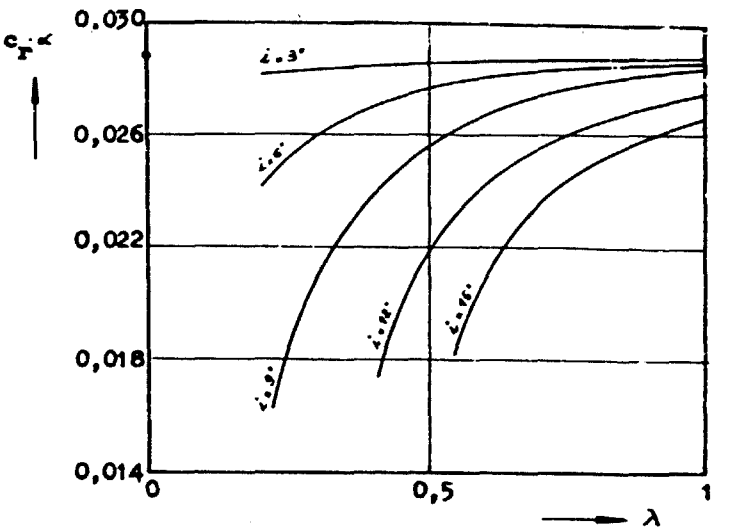

Fig. 3.24.
Variation of $c_{r,x}$ with λ for different incidences.

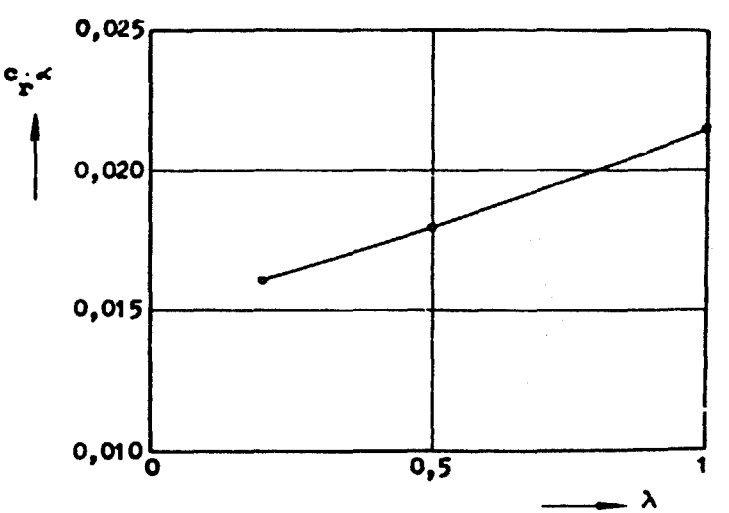

Fig. 3.25.
Variation of critical $c_{r,x}$ with λ.

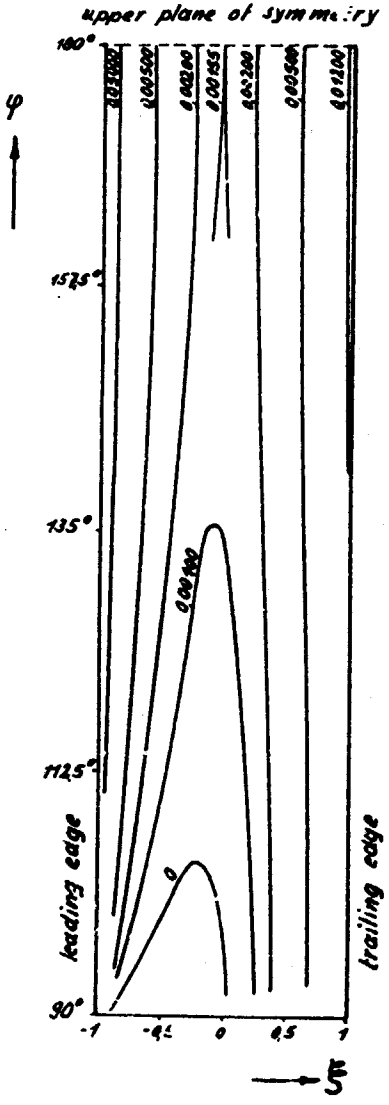

lines of iso $\frac{\partial K_p}{\partial s}$

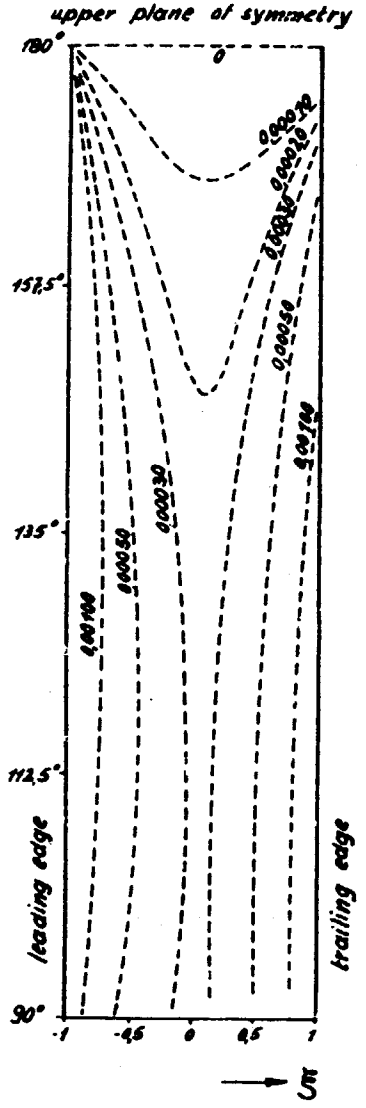

lines of iso $\frac{\partial K_p}{\partial z}$

Fig. 3.26.
$\lambda = 0{,}2$
$i = 6°$

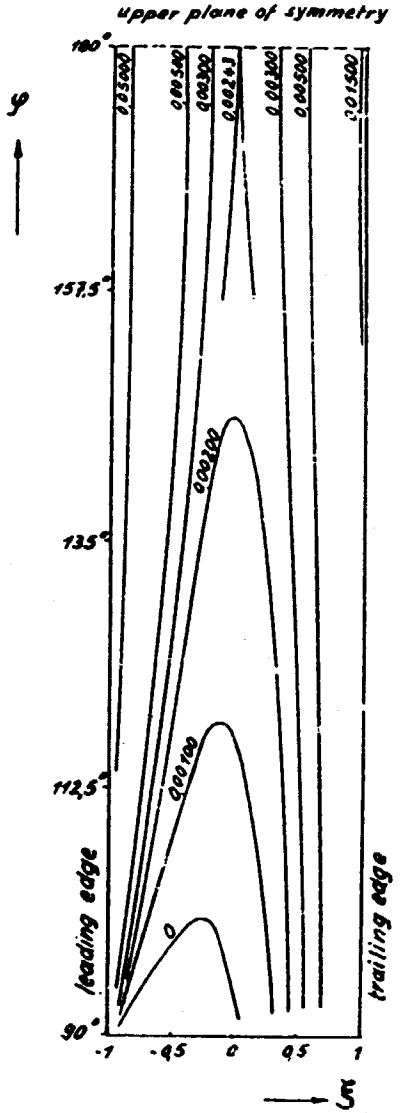

lines of iso $\frac{\partial K_p}{\partial s}$

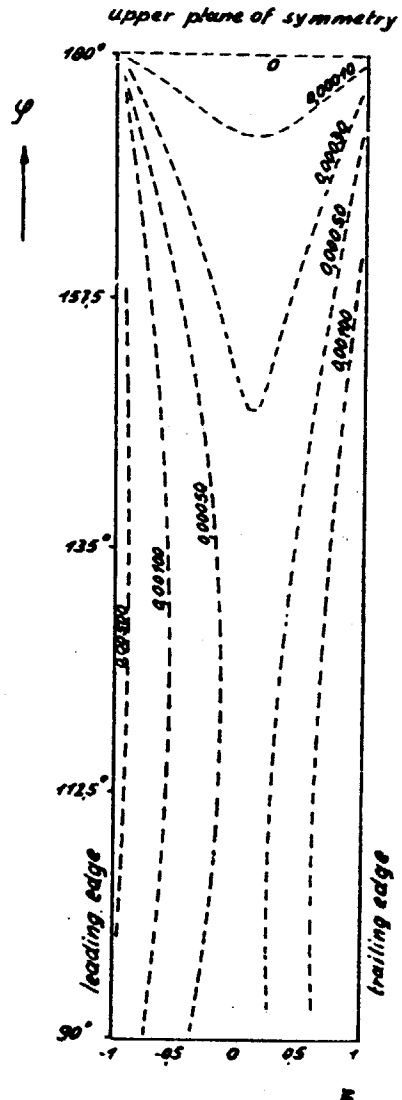

lines of iso $\frac{\partial K_p}{\partial z}$

Fig. 3.27.
$\lambda = 0{,}2$
$i = 9°$

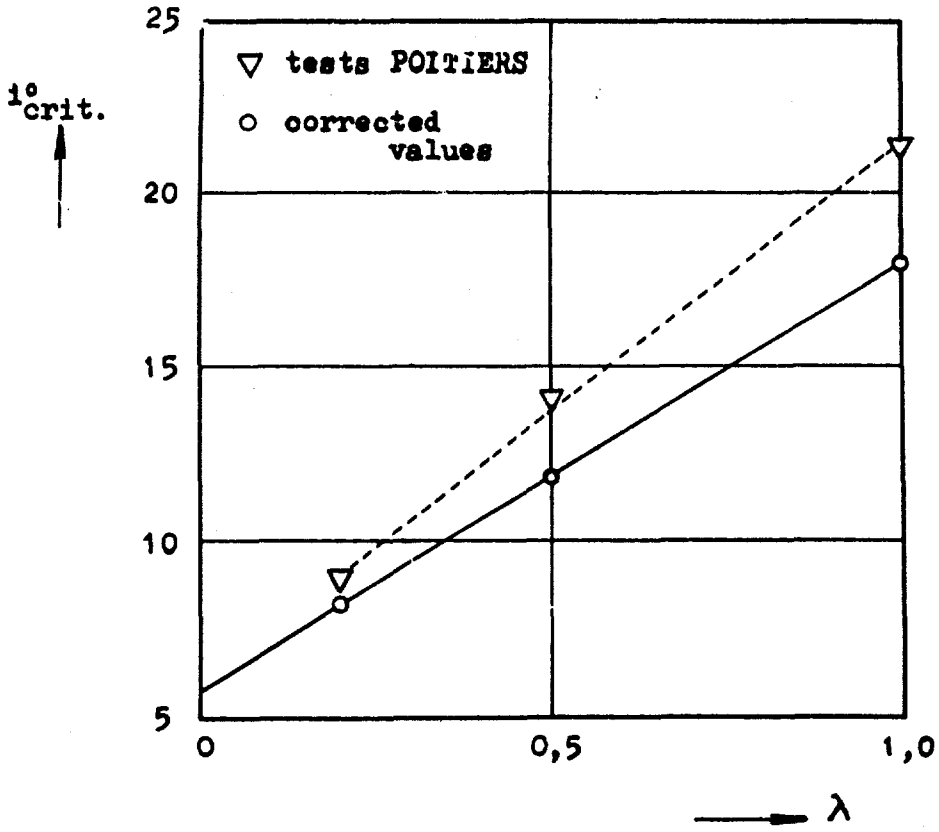

Fig. 3.28. — Variation of the critical incidences with λ

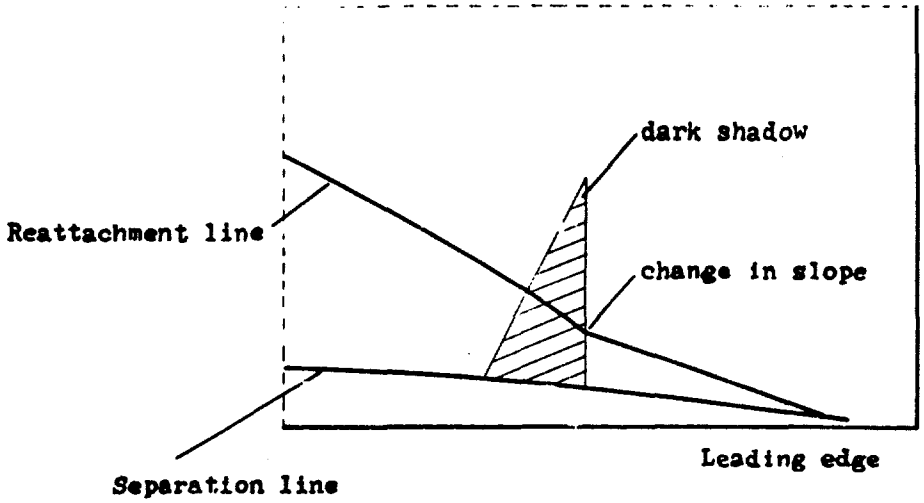

Fig. 3.29. — Principle Scheme.

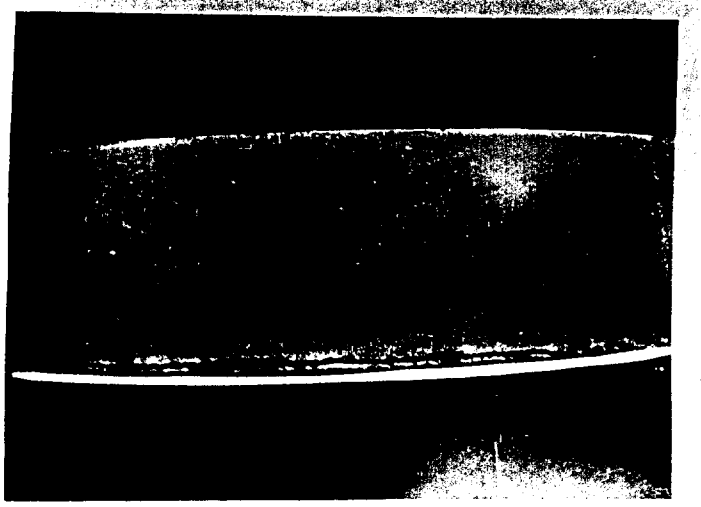

Fig. A1 $\lambda = 0.2$, $\gamma = 6^{\circ}$ Front-view

Fig. A2 $\lambda = 0.2$, $\gamma = 6^{\circ}$ Detail, $\frac{3}{4}$-Front-view from right.

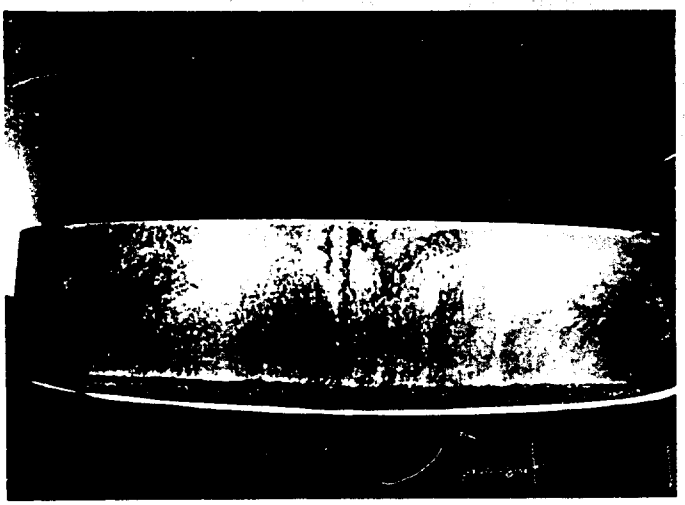

Fig. A3 $\lambda = 0.2$, $\gamma = 9^{\circ}$, Front-View seen from above

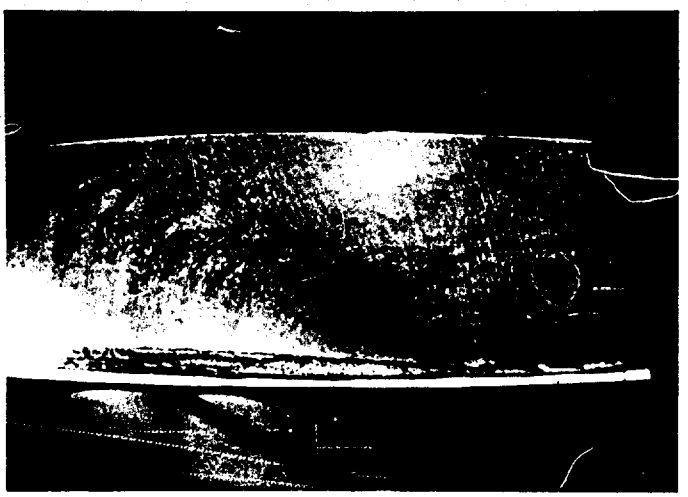

Fig. A4 $\lambda = 0.2$, $\gamma = 9^{\circ}$, $\frac{3}{4}$-Front-view from right.

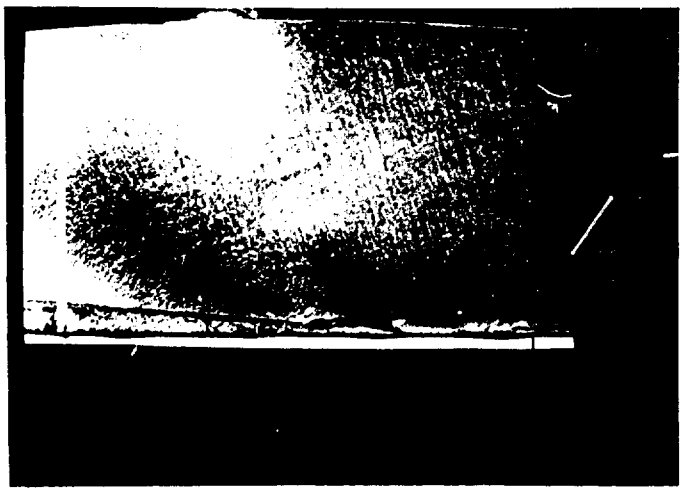

Fig. A5 $\lambda = 0.2$, $\gamma = 9^{\circ}$, Detail, $\frac{3}{4}$-Front-view from right.

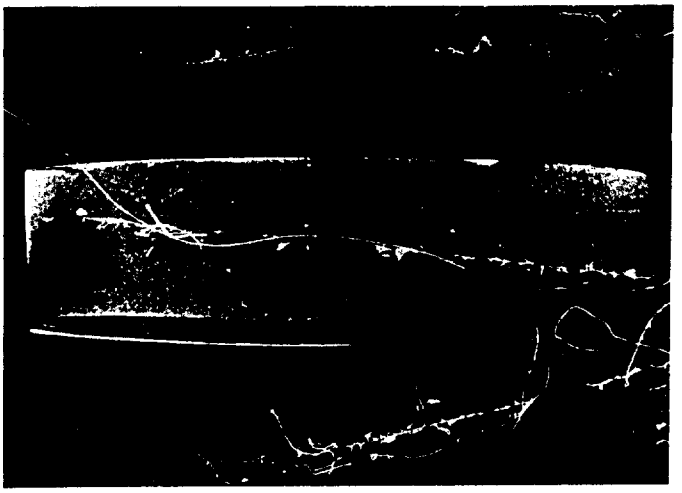

Fig. A6 $\lambda = 0.2$, $\gamma = 9.50^{\circ}$, Front-view (from above, center).

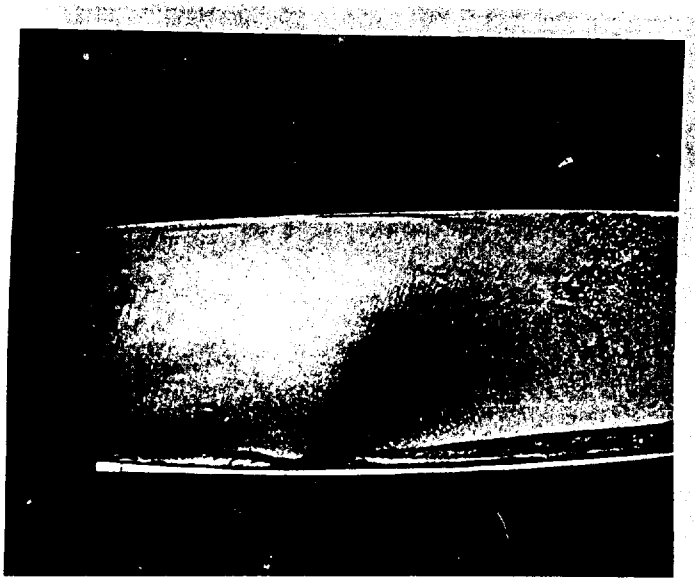

Fig. A7 $\lambda = 0{,}2$, $i = 9{,}50°$, $^3/_4$-Front-view (from left).

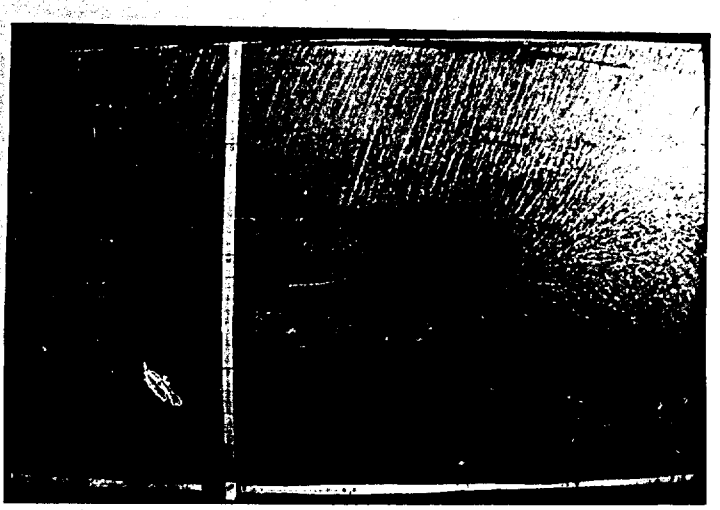

Fig. A8 $\lambda = 0{,}2$, $i = 9{,}50°$, Détail, $^3/_4$-Front-view (from left).

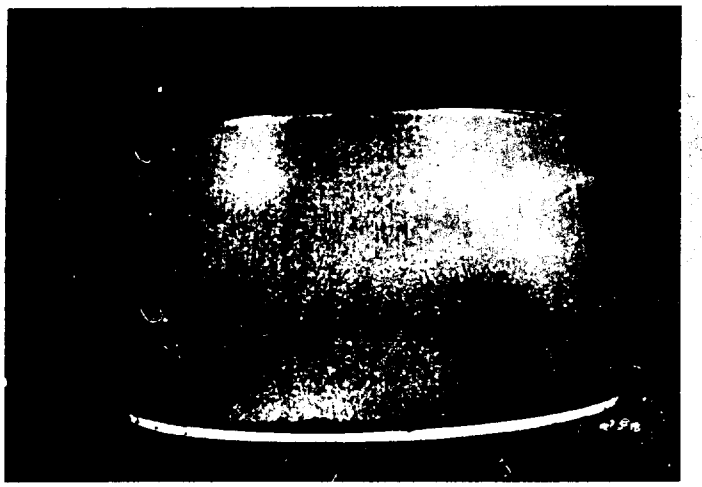

Fig. B1 $\lambda = 0{,}5$, $i = 9°$, Front-view.

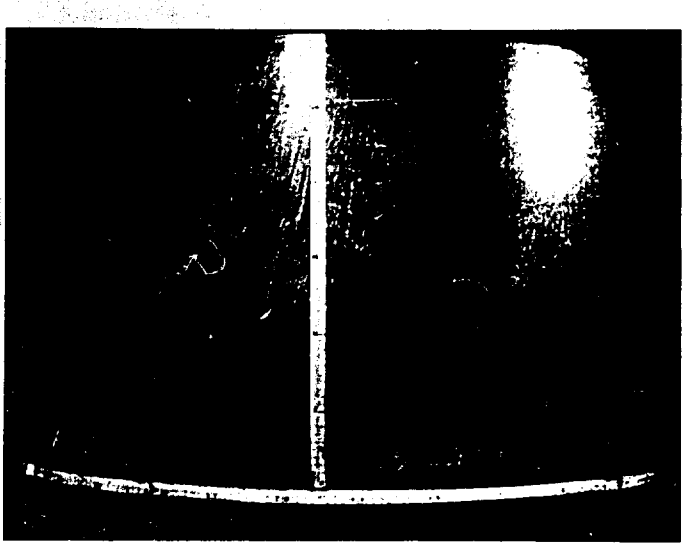

Fig. B2 $\lambda = 0{,}5$, $i = 9°$, $^3/_4$-Front-view (from left).

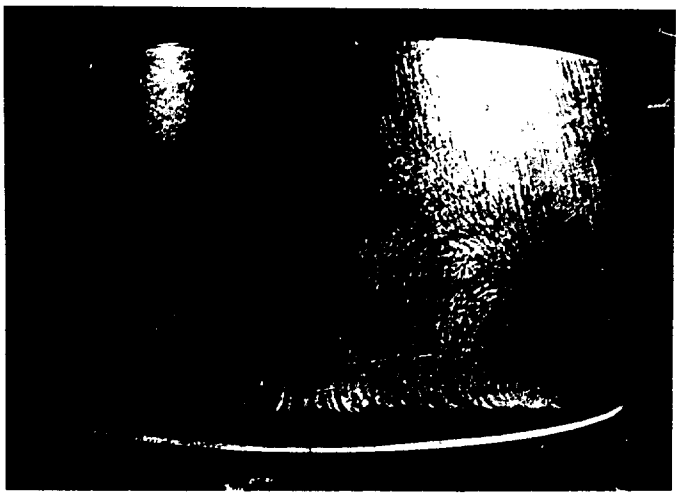

Fig. B3 $\lambda = 0{,}5$, $i = 12°$, Front-view.

Fig. B4 $\lambda = 0{,}5$, $i = 12°$, Details, $^3/_4$-Front-view (from right).

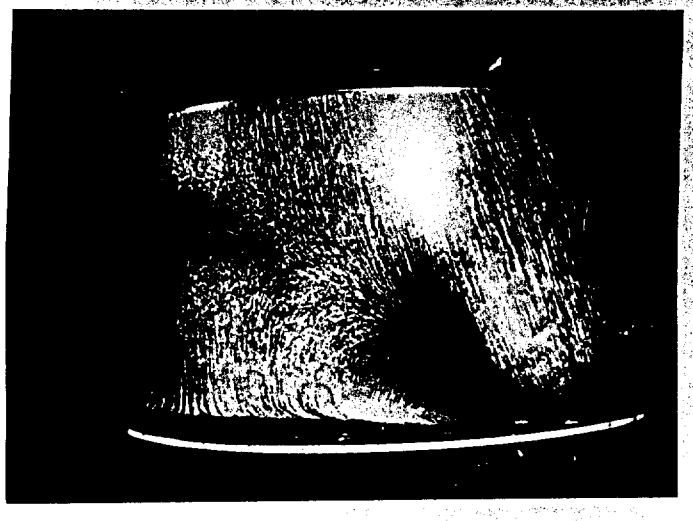

Fig. B5 $\lambda = 0,5$, $i = 12°$, $^3/_4$-Front-view (from right).

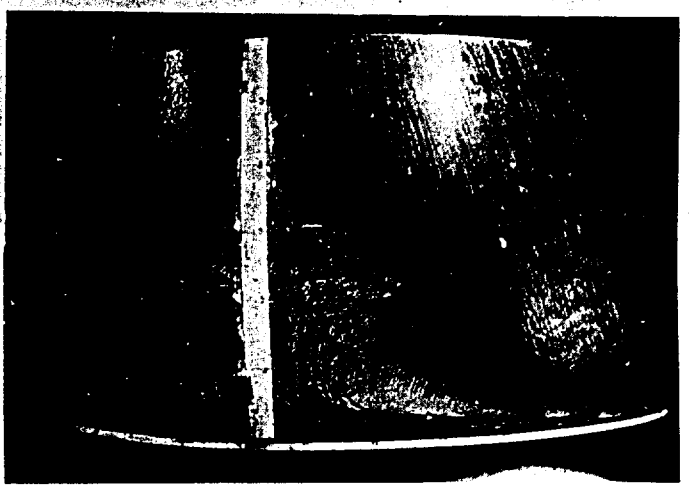

Fig. B6 $\lambda = 0,5$, $i = 12°$, $^3/_4$-Front-view (from right).

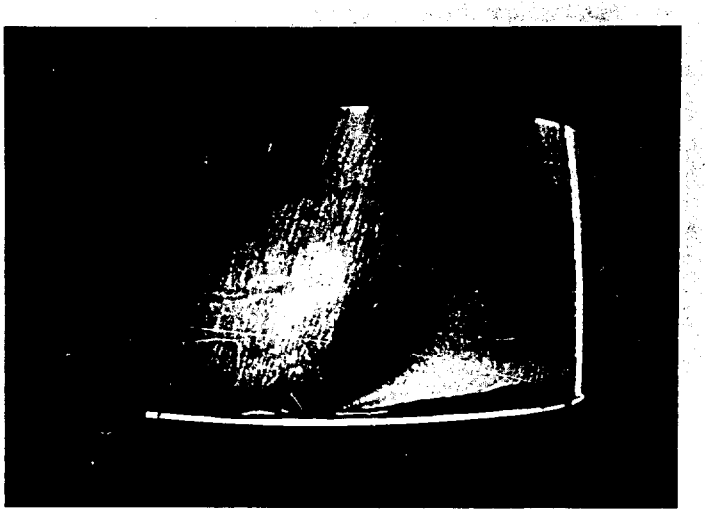

Fig. B7 $\lambda = 0,5$, $i = 12°$, $^3/_4$-Front-view (from left).

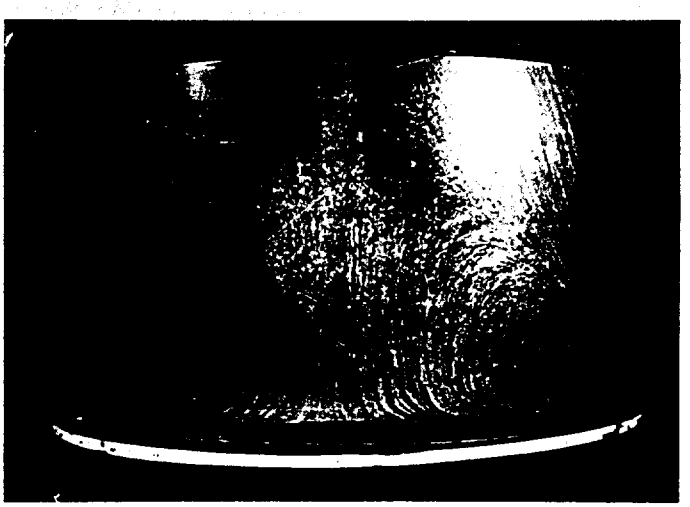

Fig. B8 $\lambda = 0,5$, $i = 13°$, Front-view.

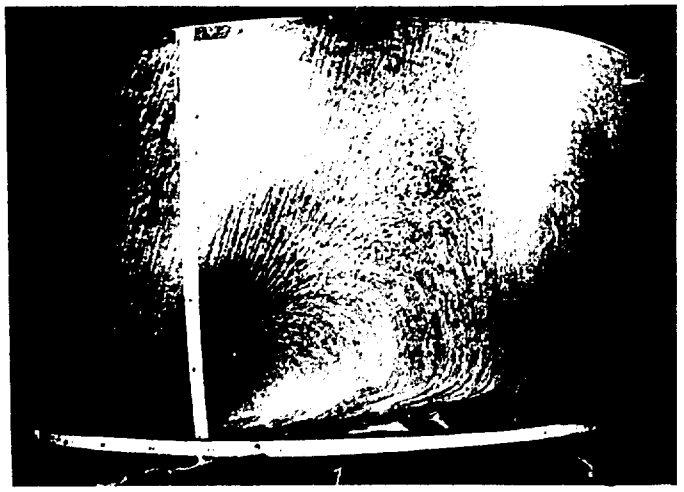

Fig. B9 $\lambda = 0,5$, $i = 13°$, $^3/_4$-Front-view (from left).

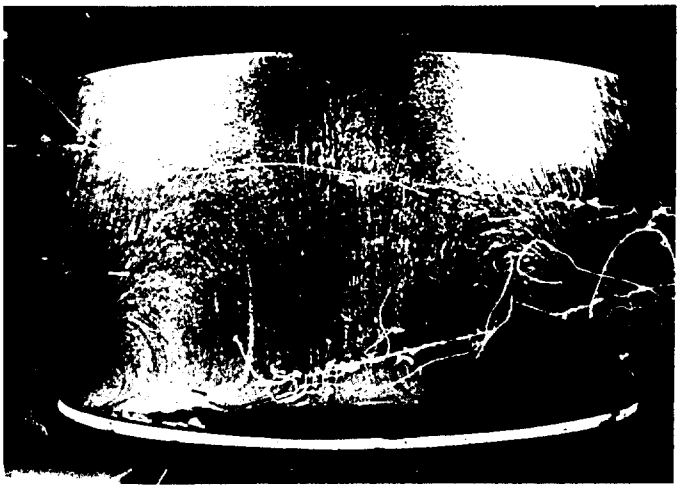

Fig. B10 $\lambda = 0,5$, $i = 13,50°$, Front-view.

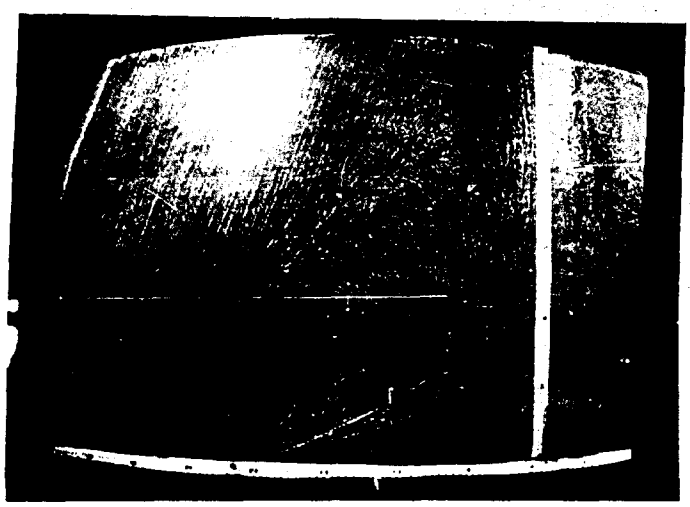

Fig. B11 z = 0.5, r = 13.50", θ_1 Front-view (from left

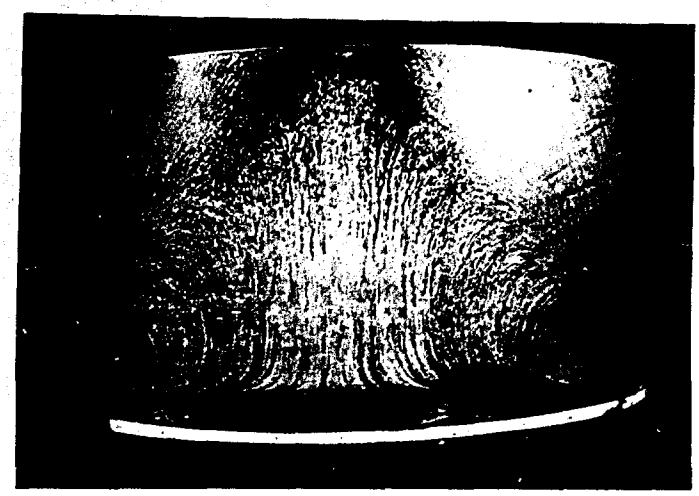

Fig. B12 z = 0.5, r = 14", Front-view.

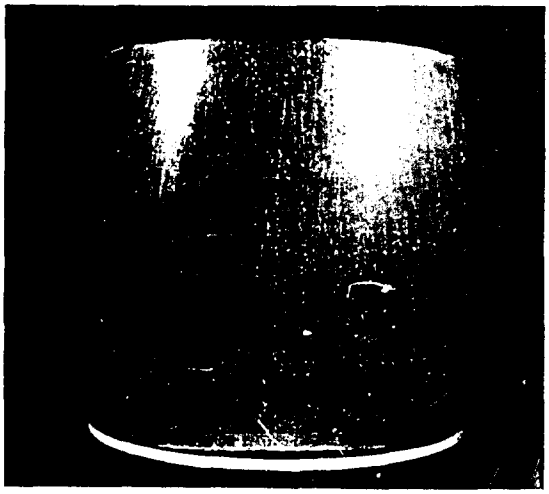

Fig. C1 z = 1, r = 9", Front-view

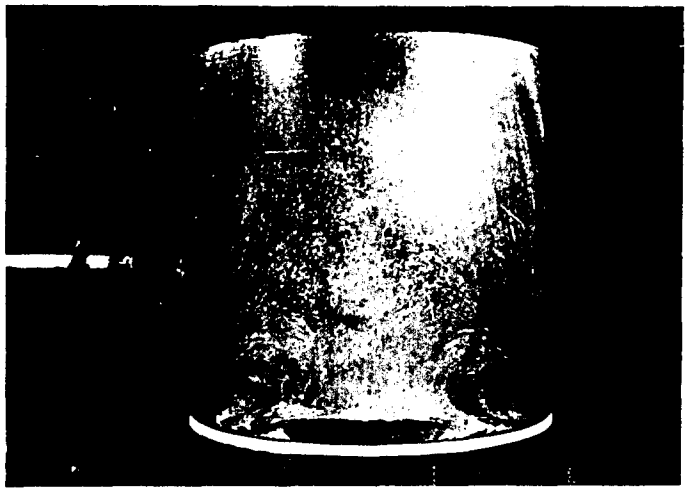

Fig. C2 z = 1, r = 15", Front-view

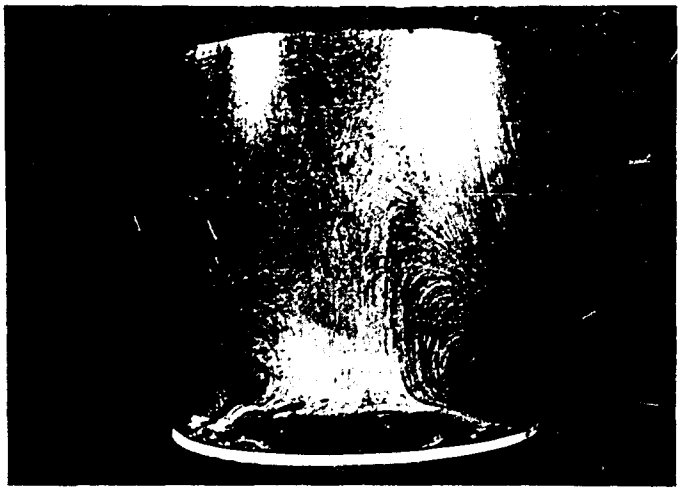

Fig. C3 z = 1, r = 18", Front-view (1st Test).

Fig. C4 z = 1, r = 18", Front-view (2nd Test).

Fig. 05 z = L / = 20%, Front view

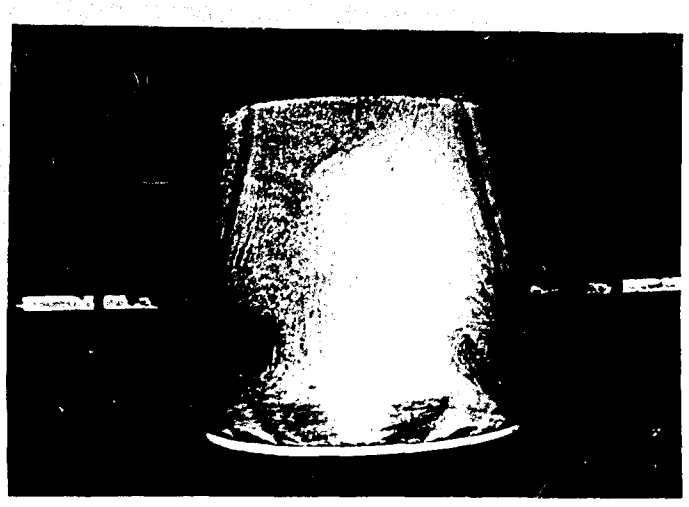

Fig. 06 z = L / = 21%, Front-view

Fig. 07 z = L / = 22%, Front view, 1st Test

Fig. 08 z = L / = 22%, Front view, Detail Trailing-Edge (1st Test).

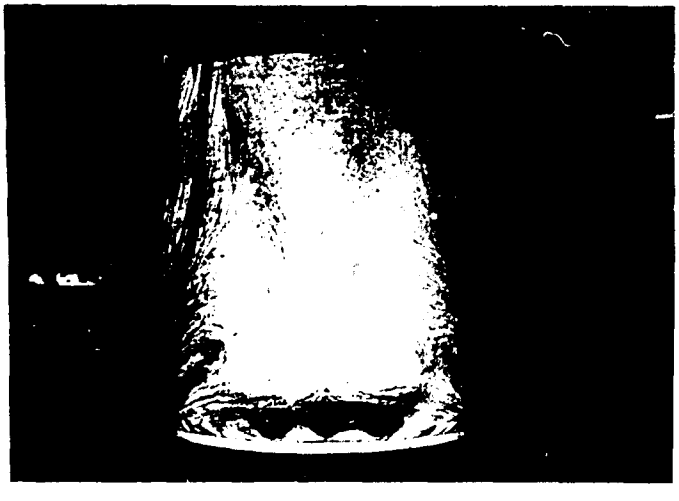

Fig. 09 z = L / = 22%, Front view, 2nd Test

Fig. 10 z = L / = 22%, Front view, Detail Trailing-Edge (2nd Test).

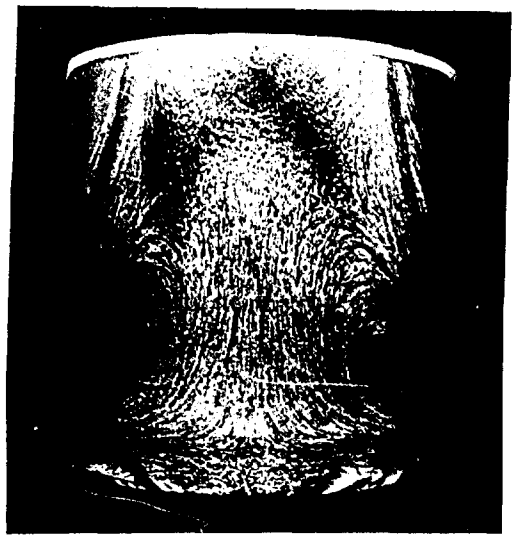

Fig. C11. $\gamma = 1$, $\gamma = 23°$.
Front-view

Fig. C12. $\gamma = 1$, $\gamma = 22°$.
Formation of the configuration (flash)

Fig. D1. $\gamma = 1$, $\gamma = 22.5°$.
Evolution of the flow configuration

Fig. D2. $\gamma = 23°$

Fig. D3. $\gamma = 24°$

$\gamma = 1$. Evolution of the flow configuration.

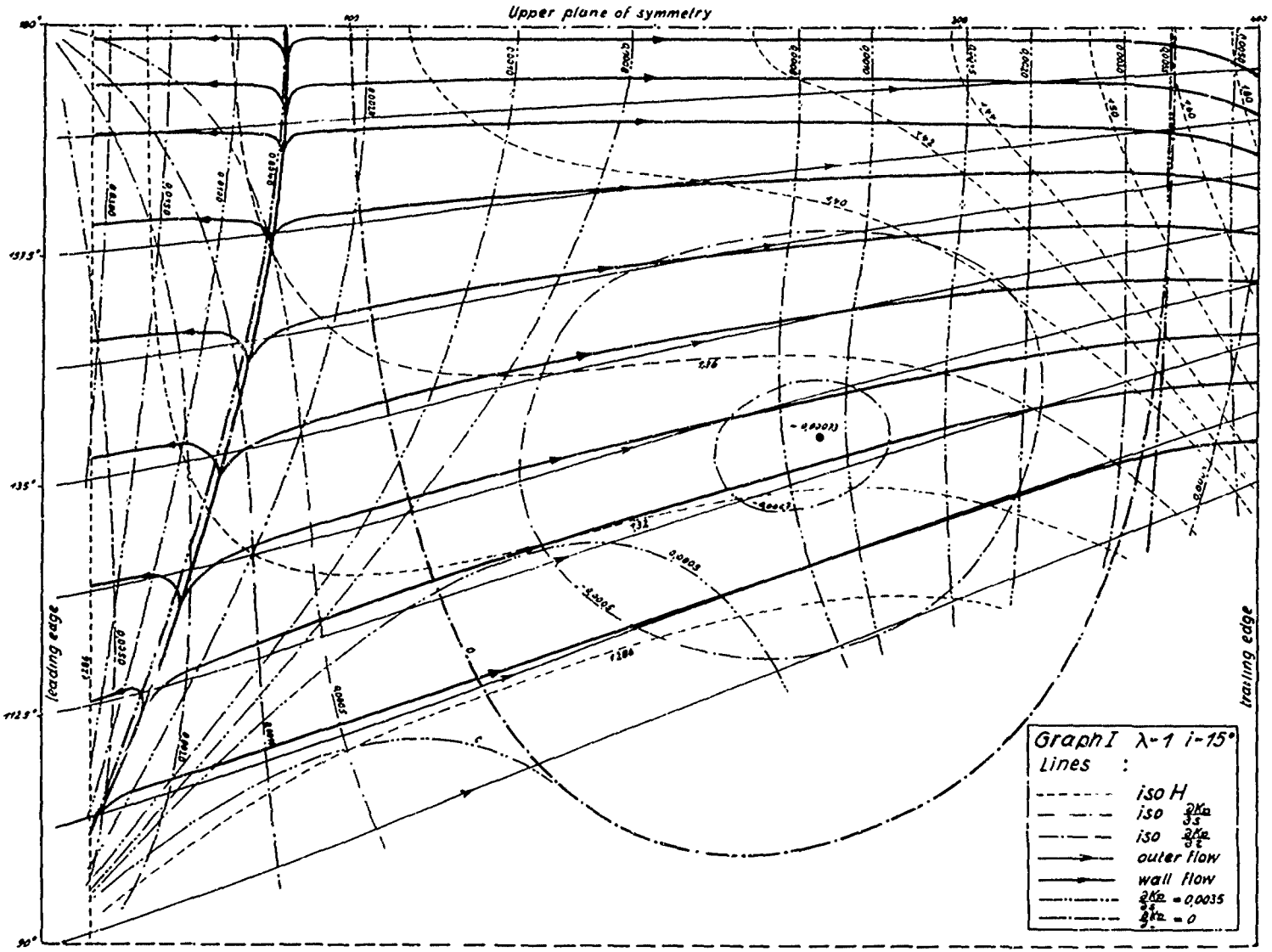
Upper plane of symmetry
leading edge
trailing edge
180°
151.5°
135°
112.5°
90°
Graph I λ=1 i=15°
Lines :
iso H
iso 2Kp/3s
iso 2Kp/3t
outer flow
wall flow
2Kp/3t = 0,0035
2Kp/3t = 0

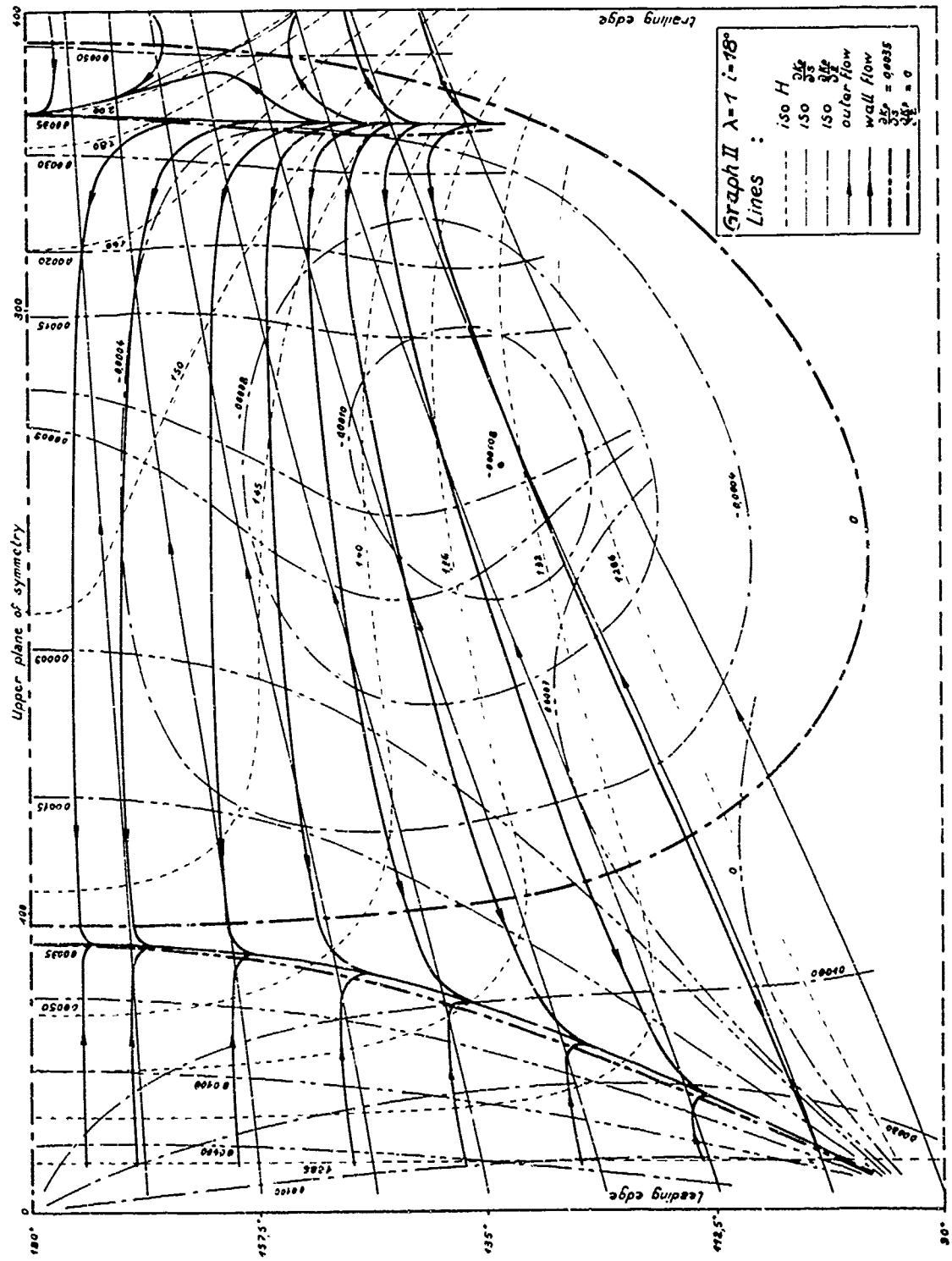
Graph II λ=1 i=18°
Lines :
iso H
iso
iso
outer flow
wall flow
= 0
trailing edge
leading edge
Upper plane of symmetry
180°
157,5°
135°
112,5°
90°

ERRATA

page	instead of :	one should read :
6, § 1.4.1.1., (*)	$C_1 = \left\{ \frac{1}{2} c_{fl} \left[\int_0^{x_t/l} \left(\frac{U_e}{U} \right) \cdot \left(\frac{R}{R_0} \right)^2 d \left(\frac{x}{l} \right) \right]^{\frac{1}{2}} \right\}^{\frac{n+1}{n}}$	$C_1 = \left\{ \frac{1}{2} c_{fl} \left[\int_0^{x_{tr}/l} \left(\frac{U_e}{U_\infty} \right)^5 \left(\frac{R}{R_0} \right)^2 d \left(\frac{x}{l} \right) \right]^{\frac{1}{2}} \right\}^{\frac{n-1}{n}}$
	x_t = transition point	x_{tr} = transition point
11, § 3.1.7.	mean induced velocity c_{φ_1}	mean induced velocity $\bar{c}_{\varphi_1}$
14, § 3.9.2.1.	111/4°	11 ¼°
15, § 3.9.3.	for i = 21°	for i_g = 21°
16, § 3.12.1.2.	($\mathcal{R}_{\delta_1}$ > 450)	($\mathcal{R}_{\delta_1}$ > 450)
18, Symbols	$\mathcal{R}\delta$	$\mathcal{R}_\delta$
	$\mathcal{R}_s$ Reynolds number based on the local distance $\mathcal{R}\delta = \frac{U_e s}{\nu}$	$\mathcal{R}_s$ Reynolds number based on the local distance $\mathcal{R}_s = \frac{U_e \cdot s}{\nu}$
21, Table 3.2.1.	$U_\infty \approx$ 45 ms	$U_\infty \approx$ 45 m/s
29, Fig. 3.2.	$t(\xi) = \sum_{j=1}^{6} t_j \cdot \sin j$	$t(\xi) = \sum_{j=1}^{6} t_j \cdot \sin j\vartheta$
30, Fig. 3.4.	i = 18°	i = 9°
34, Fig. 3.13.	$A = q_\infty \cdot S \cdot c' \cdot i$	$A = q_\infty \cdot S \cdot c_l' \cdot i$